 doi:10.20944/preprints201811.0192.v1

Article

A Combined Geochemical and Fluid Inclusion Study of the Hongyan Cu-Polymetallic Deposit in the Eastern Hegenshan-Heihe Suture Zone, NE China: Implications for Petrogenesis, Tectonic Setting and Mineralization

Chen Mao [1], Xinbiao Lü [1,2]* and Chao Chen [2]

[1] Faculty of Earth Resources, China University of Geosciences, Wuhan 430074, China; maochen_110@cug.edu.cn (C.M.)
[2] Institute of Geological Survey, China University of Geosciences, Wuhan 430074, China; chenchao_109@163.com (C.C)
* Correspondence: luxb@cug.edu.cn; Tel.: +86-159-7293-4906

Abstract: In order to study the petrogenesis and tectonic setting of Permian A-type granites and their relationships with hydrothermal mineralization along the Hegenshan-Heihe suture zone (HHSZ) in northeastern China, we select the newly discovered Hongyan Cu-polymetallic deposit in the northeastern part of the HHSZ that develops three stages of mineralization associated with the Shanshenfu alkali-feldspar granite (SAFG). The zircon U-Pb dating and whole rock geochemistry suggest that the SAFG is a typical A-type granite formed in the Early Permian. The zircon Hf isotopes and trace elements suggest that the SAFG has high Ti-in-zircon temperature (721–990℃), high magmatic oxygen fugacity and largely positive $\varepsilon_{Hf}(t)$ (+6.0 to +9.9). Therefore, we propose that the SAFG was derived from the crustal assimilation and fractional crystallization of the charnockitized juvenile crust. The high oxygen fugacity favors the chalcophile elements (e.g., Cu, Au, Ag) of the source region enriched in the fluid phases after magmatic fractional crystallization, consequently facilitating subsequent hydrothermal mineralization, which is also consistent with the characteristics of ore-forming fluids that changed from the initial high temperature, high salinity, high fO_2 and CO_2-rich magmatic-hydrothermal fluids of stage I to CO_2-poor, dilute, and cooling meteoric fluids of stage III. Combined with regional geological background, the Permian A2-type granites along the HHSZ can be formed in post-collisional slab break-off process. In subsequent exploration for hydrothermal deposits along the HHSZ, the Permian A-type granites with arc-related juvenile crustal source and high fO_2 have great potential and need more attention.

Keywords: Hegenshan-Heihe suture zone; Permian A-type granite; granite petrogenesis; Hongyan Cu-polymetallic deposit; ore-forming fluids; post-collisional slab break-off

1. Introduction

Since the introduction of A-type granites by Loiselle and Wones [1], they have been studied extensively by domestic and foreign scholars due to their important geodynamic significance, complicated petrogenesis and economic potential [2–6]. In northeastern China (NE China), numerous Permian A-type granites (260 ~ 300 Ma) have been identified along the Hegenshan-Heihe suture zone (HHSZ) in the past two decades (Figure 1a, b) [3,4,7–10], which belongs to the eastern part of the very large A-type granite belt that extends from northern Xinjiang, via Mongolia to NE China (Figure 1a) and is produced along the Central Asian Orogenic Belt (CAOB). The previous

studies have provided mineralogical and geochemical constraints on the types (A2 type), sources (crust-mantle mixing or crustal sources) and tectonic settings (post-orogenic extension or post-collisional extension) of the Permian A-type granites along the HHSZ [3,4,7–10]. In addition, more and more newly discovered hydrothermal deposits are associated with these Permian A-type granites, including Aoyoute Cu-polymetallic deposit (287Ma), Bayandulan Cu-polymetallic deposit (284Ma) and Ataiwula Cu-polymetallic deposit (276Ma) [10]. Thus, the petrogenesis and tectonic setting of these A-type granites and their relationships with hydrothermal mineralization become the urgent questions that need to be answered, due to their important geological significance, not only for the regional tectonic evolution, but also for exploring more related hydrothermal deposits in the region. However, few studies have been carried out on the relationship between the petrogenesis and tectonic setting of these Permian A-type granites and hydrothermal mineralization.

The newly discovered Hongyan Cu-polymetallic deposit is located in the northeastern part of the HHSZ (Figure 1c), and develops Cu-polymetallic mineralization associated with Permian A-type granite. Thus, the deposit provides a good opportunity to study the petrogenesis and tectonic setting of A-type granite and its relationships with the ore-forming fluids. In recent years, the studies on the origin and oxidation state of ore-related granites and their relationships with metallogenic process have become mainstream [11–16]. The zircon geochemistry has been widely applied to analyze the temperature and oxygen fugacity (fO_2) of magma sources [17–20], the composition of parental melts [21–22], source-rock type and crystallization environment [23–25], because of zircon's refractory nature and low elemental diffusivities [26], which can provide powerful evidences for demonstrating the petrogenesis of A-type granites and their influence (e.g., magma sources and fO_2) on the geochemical behavior of certain metal elements (e.g., Cu and Au) in melt [27–30]. Moreover, Fluid inclusions during mineralization processes also provides critical information on the physico-chemical nature of ore-forming fluids and their relationships with ore-related granites in hydrothermal deposits [31–33]. In this paper, we present zircon U-Pb ages, trace elements and Hf isotope data, whole-rock major and trace element data of the Permian A-type granite in the Hongyan Cu-polymetallic deposit, to discuss its oxidation state and petrogenesis, and then coupled with analyzing fluid inclusion for each minerlization stage, to determine the relationships between ore-forming fluids and A-type granite, and their tectonic setting. We believe that the results would be significant, not only for providing new insights into the relationships between A-type granites and related hydrothermal mineralization, but also for exploring more hydrothermal deposits associated with Permian A-type granites in the region.

Preprints (www.preprints.org) | NOT PEER-REVIEWED | Posted: 8 November 2018 doi:10.20944/preprints201811.0192.v1

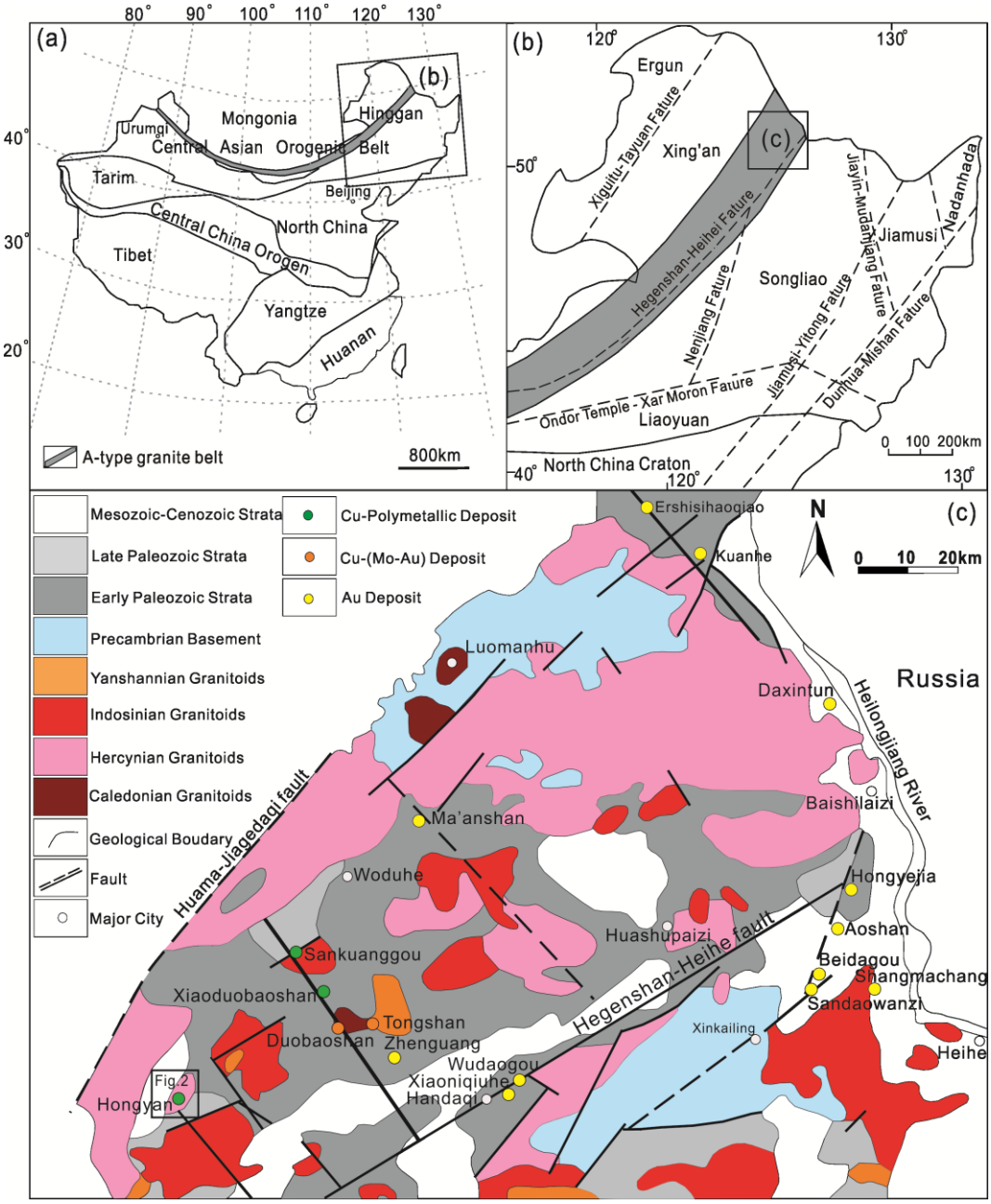

Figure 1. (a) Geotectonic division of China (after Mao et al. [34]); (b) Tectonic subdivisions of the northeast China (after Wu et al. [35]); (c) Regional geological map of the northern Xing'an Block (after Gao et al. [36]).

2. Regional Geology

The Xing-Meng Orogen Belt is located in the eastern part of the CAOB, and was formed in the Permian through the collision between the Siberia block and North China block (Figure 1a) [35,37,38], which is further subdivided by several NE-striking faults into different microcontinental massifs or terranes, including the Ergun massif, the Xing'an terrane, the Songliao terrane, the Jiamusi terrane and the Liaoyuan terrane (Figure 1b). These terranes have undergone the superposition of EW-trending tectonic evolution of the Paleo-Asian Ocean during the Paleozoic and NNE-trending tectonic evolution of the western Pacific Ocean during the Mesozoic and Cenozoic.

The HHSZ represents a suture zone resulting from the collision of the Xing'an and Songliao terranes (Figure 1b). The outcropping strata in the Xing'an terrane and its adjacent area can be

approximately divided into four units (Figure 1c) [39,40]: (1) Sporadic distribution of Precambrian crystalline basement rocks composed of granulites, gneisses and schists; (2) Extensive exposure of Early Paleozoic metamorphosed volcanic and sedimentary rocks consisting of schist, sandy slate, marble, and andesite, which are formed in continental margin and arc accretion settings; (3) The Late Paleozoic units are similar to the Early Paleozoic units but with lower metamorphic grades; and (4) Mesozoic continental intermediate-felsic volcanic and sedimentary rocks, and Cenozoic sedimentary basin strata. NNE-trending Paleozoic batholith-shaped granitoid rocks have a discontinuous zonal distribution on the north side of the HHSZ (Figure 1c), which is the evidence for the strong transformation of Mesozoic tectonic-magmatic activity [4,41].

Intense hydrothermal activity was associated with these periods of magmatism, and resulted in various types of hydrothermal deposits, primarily including skarn Cu-polymetallic deposits (e.g., Sankuanggou and Xiaoduobaoshan), porphyry Cu-(Mo-Au) deposits (e.g., Duobaoshan and Tongshan), and epithermal Au deposits (e.g., Shangmachang, Beidagou, Sandaowanzi, Tianwangtaishan and Zhenguang) (Figure 1c) [36,42,43], which constitute the northeastern segment of the Xing'an Cu-Mo-Fe-Pb-Zn-Au belt, and is considered to be one of the most important areas in the Great Xing'an Range metallogenic province [39, 44]. These deposits are located in a nearly NE-trending band along the HHSZ and its secondary NE- and NW-trending faults that are the main ore-controlling structures in this region (Figure 1c).

3. Deposit Geology

The Hongyan Cu-polymetallic deposit (E125°01′28″ to 125°06′30″, N49°33′30″ to 49°42′30″; Figure 2) is located in the northeastern part of the HHSZ (Figure 1c). Paleozoic and Mesozoic volcanic rocks are widespread in the deposit (Figure 2). Paleozoic volcanic rocks mainly include the Upper Carboniferous–Lower Permian Baoligaomiao Formation (C_2P_1bl) that is a suite of continental volcanic rocks composed of rhyolitic tuff, andesitic tuff and basalt. Mesozoic volcanic rocks are subdivided into the Lower Jurassic Manitu Formation (J_3mn), the Upper Cretaceous Baiyingaolao Formation (K_1b) and Damoguaihe Formation (K_1d). The Manitu Formation is mainly composed of dacitic ignimbrite and dacite. The Baiyingaolao Formation is mainly composed of rhyolite, rhyolitic volcanic breccias, and rhyolitic ignimbrite. The Damoguaihe Formation is mainly composed of conglomerate, fine sandstone, and tuff breccias. Structures are dominated by the NE-trending faults (e.g., F1 and F2), NW-trending faults (e.g., F3, F4, F5, F6, F7 and F9) and nearly EW-trending faults (e.g., F8). Magmatic rocks are dominated by the Shanshenfu alkali-feldspar granite (SAFG) with an area of ~75 km^2, which intrudes into Paleozoic volcanic rocks with irregular contact relationship, and is covered by Mesozoic volcanic rocks and Quaternary (Figure 2). According to the grain size, the SAFG can be subdivided into two phases, the inner phase and outer phase, and their boundaries are gradational (Figure 2). The SAFG consists of subhedral alkali feldspar (50–55 vol%), anhedral quartz (30–35 vol%), plagioclase (5–10 vol%), sericite (1–5 vol%) (Figure 4a, b) and minor accessory minerals including magnetite (Figure 4d), zircon and titanite.

Preprints (www.preprints.org) | NOT PEER-REVIEWED | Posted: 8 November 2018 doi:10.20944/preprints201811.0192.v1

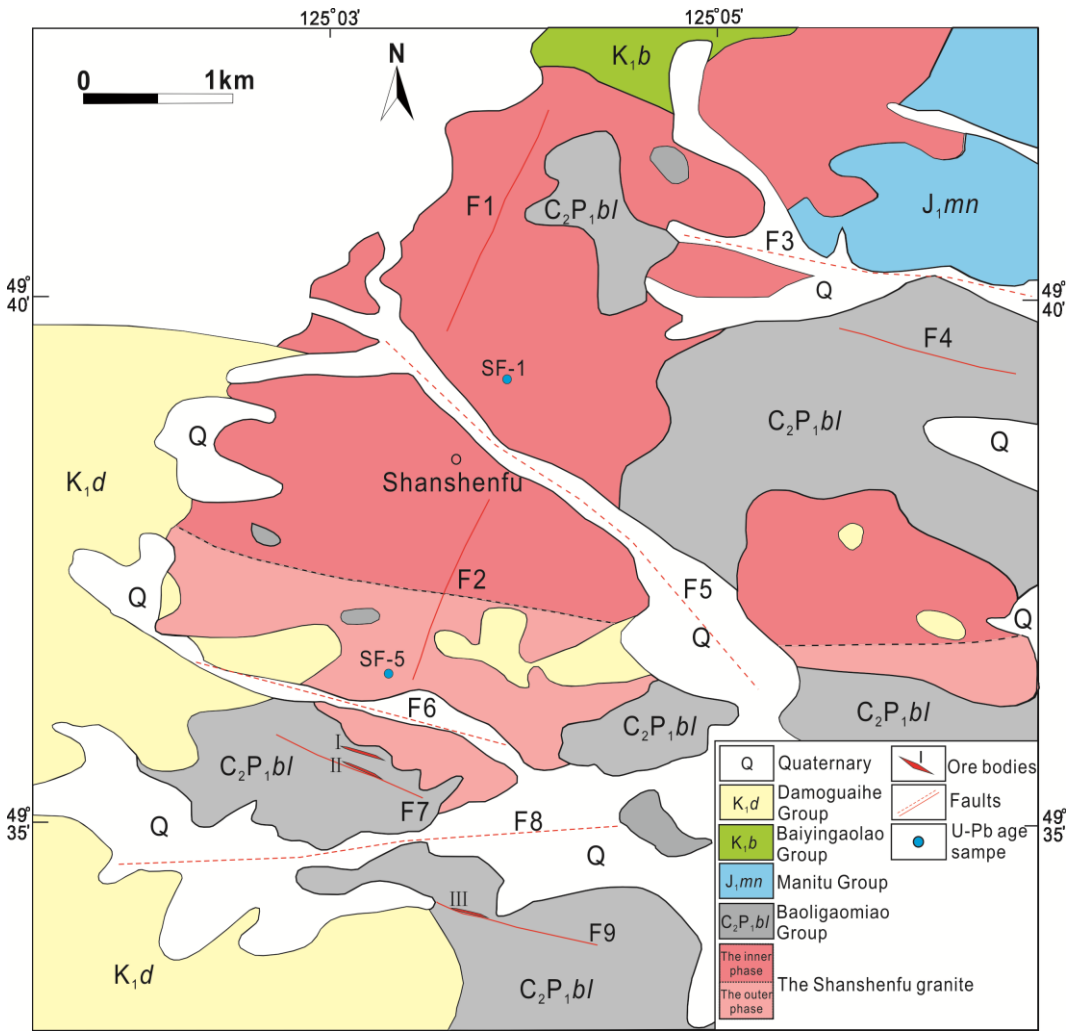

Figure 2. Geological sketch of the Hongyan Cu-polymetallic deposit.

4. Mineralization and alteration

The SAFG is pervasively altered by potassic and quartz-sericite alterations (Figure 4c), accompanied by some disseminated Cu mineralization (Figure 4d). Cu-polymetallic mineralization generally occurs as veins and veinlets in the Baoligaomiao Formation close to its southern contact zone with the SAFG, which is structurally controlled by NW-striking faults (Figure 2). Three mineralized bodies have been identified in the Hongyan deposit (Figure 2). The No. I ore body exhibits a length of 250 m, an average thickness of 3.1 m, and Cu grades of 0.5–1.5%. The length of No. II ore body is 220 m, with an average thickness of 2.3 m, and Cu, Au and Ag grades of 0.4–1.2%, 0.34–2.21 g/t and 0.76–21.6 g/t, respectively. The No. III ore body has a length of 215 m, an average thickness of 1.8 m, and contains Cu, Au and Ag grades of 0.5–1.35%, 0.27–2.62 g/t and 0.64–16.2 g/t, respectively.

Based on our geological field investigation and petrographic observation, metal minerals mainly consist of chalcopyrite and pyrite, with minor bornite, covellite, galena, sphalerite and magnetite. Gangue minerals are dominated by quartz, K-feldspar, sericite, muscovite, chlorite, epidote, calcite and fluorite. The silicification are well developed and closely related to sulfide mineralization. Based on mineral assemblages and associated hydrothermal alteration minerals, we can identify three stages of mineralization (Figure 5): quartz ± K-feldspar ± pyrite (stage I), quartz +

 doi:10.20944/preprints201811.0192.v1

chalcopyrite ± pyrite ± bornite ± sphalerite ± galena (stage II) and quartz + carbonate ± fluorite (stage III). Stage I is defined by the occurrence of quartz and K-feldspar with minor pyrite and magnetite as veins (Figure 3e and 4e). Stage II is represented by the widespread occurrence of quartz, chalcopyrite and pyrite minerals as veins or veinlets with minor bornite, covellite, galena and sphalerite (Figure 3d–g and 4f–h). Chalcopyrite replaces early bornite and commonly intergrown with pyrite and galena（Figure 4g and 4h）. Chalcopyrite and pyrite are partly replaced by the covellite (Figure 4f). Gold mineralization is most commonly hosted within sulfide minerals in this stage, and visible gold can be found in the quartz veins (Figure 4i). Stage III is characterized by the appearance of calcite and quartz with minor fluorite as veins or veinlets (Figure 3h–i). Small amounts of pyrite occur in quartz-calcite veins, and gold mineralization is less in this stage.

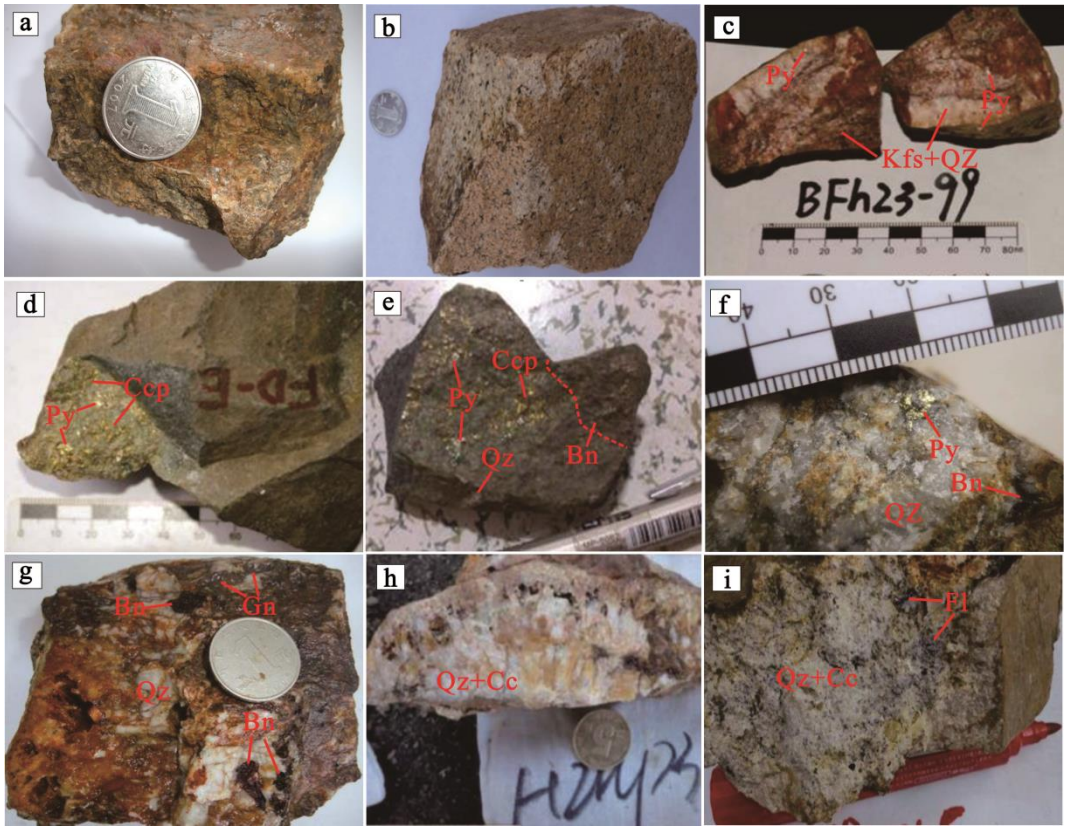

Figure 3. Hand specimen photos of the Shanshenfu alkali-feldspar granite and Stage I–III mineralization from the Hongyan Cu-polymetallic deposit. (a) Medium-grained alkali-feldspar granite (the inner phase); (b) Fine-grained alkali-feldspar granite (the outer phase); (c) Stage I K-feldspar–quartz–pyrite vein; (d) Stage II disseminated chalcopyrite–pyrite–quartz mineralization; (e) Stage II quartz–pyrite–chalcopyrite–bornite vein; (f) Stage II quartz–pyrite–bornite vein; (g) Stage II quartz–bornite– galena vein; (h) Stage III quartz–calcite vein; (i) Stage III quartz–calcite–fluorite vein. Qz=quartz, Kf=K-feldspar, Py=pyrite, Ccp=chalcopyrite, Bn=bornite, Gn=galena, Cc=calcite, Fl=fluorite.

 doi:10.20944/preprints201811.0192.v1

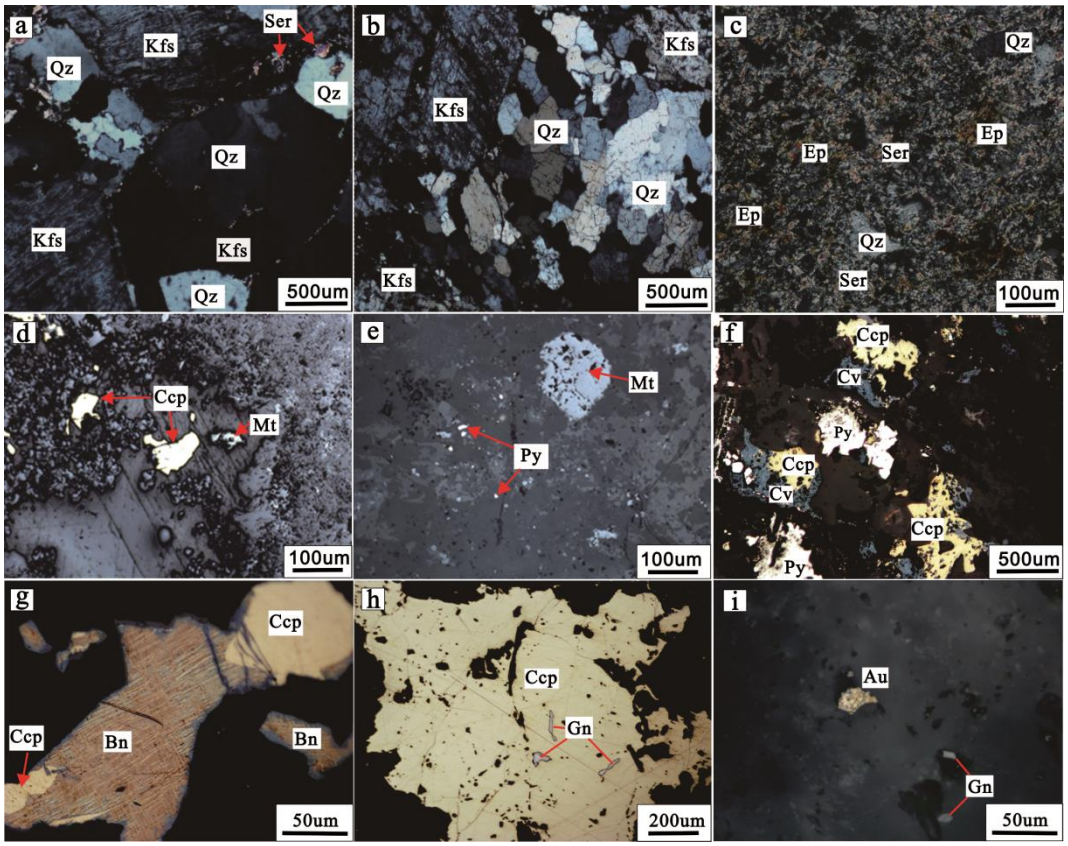

Figure 4. Photomicrographs of the Shanshenfu alkali-feldspar granite, hydrothermal alteration features and metal mineral assemblages. (a) Medium-grained alkali-feldspar granite (the inner phase); (b) Fine-grained alkali-feldspar granite (the outer phase); (c) Widespread alteration of quartz, sericite and epidote in the granite; (d) Chalcopyrite and magnetite in fine-grained alkali-feldspar granite (the outer phase); (e) Pyrite and magnetite in Stage I K-feldspar–quartz–pyrite vein; (f) Chalcopyrite intergrown with pyrite replaced by the covellite in Stage II quartz vein; (g) Chalcopyrite replace bornite in Stage II quartz vein; (h) Chalcopyrite intergrown with galena in Stage II quartz vein; (i) Visible gold intergrown with galena in Stage II quartz vein. Py=pyrite, Ccp=chalcopyrite, Bn=bornite, Gn=galena, Mt=magnetite, Cv=covellite, Au=native gold, Qz=quartz, Kf=K-feldspar, Ser=sericite, Ep= epidote.

Preprints (www.preprints.org) | NOT PEER-REVIEWED | Posted: 8 November 2018 doi:10.20944/preprints201811.0192.v1

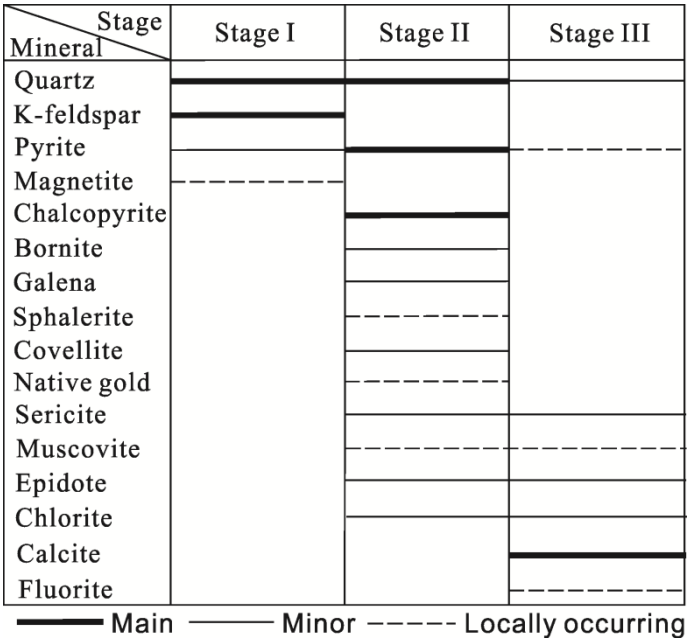

Figure 5. Paragenetic sequence for the Hongyan Cu-polymetallic deposit.

5. Analytical methods

5.1. Zircon U-Pb dating analysis

The sample SF-1 from the inner phase and the sample SF-5 from the outer phase were collected for geochronology (Figure 2). Zircon grains were separated from two representative samples using conventional heavy liquid and magnetic techniques, and then handpicked under a binocular microscope. Handpicked zircon grains were mounted on adhesive tape, then enclosed in epoxy resin and polished to section the crystals in about half for analysis. Reflected and transmitted light microscopy and cathodoluminescence (CL) images were made at the State Key Laboratory of Geological Processes and Mineral Resources, China University of Geosciences, Wuhan, to study interior textures of zircons. Zircon U-Th-Pb measurements were done under 32 um diameter laser beam at the same laboratory using a Geo-Las 2005 System. An Agilent 7500a ICP-MS instrument was used to acquire ion-signal intensities with a 193 nm ArF-excimer laser and a homogenizing, imaging optical system (MicroLas, Göttingen, Germany). Detailed instrumentation and analytical accuracy description were given by Liu et al. [45,46]. Time-dependent drifts of U-Th-Pb isotopic ratios were corrected using a linear interpolation (with time) for every six analyses according to the variations of external standard zircon 91500 (2 zircon 91500 + 6 samples + 2 zircon 91500) [46]. The ages were calculated by inhouse software ICPMSDataCal (ver 6.9, China University of Geosciences) [45] and concordia diagrams were made by Isoplot/Ex ver3.0 [47]. Trace element compositions of zircon were calibrated against GSE-1G combined with internal standardization 29Si [46].

Zircon Ce and Eu anomalies, Ti-in-zircon temperatures and magmatic oxygen fugacity (fO_2) were calculated using the trace element compositions of zircons collected during the same analysis interval as U-Pb dating. The method for calculating these parameters has been described in Ferry and Watson [18], and Trail et al. [19,20]. CGDK software [48] was used for plotting data.

5.2. Zircon Lu-Hf isotopes analysis

 doi:10.20944/preprints201811.0192.v1

In-situ zircon Hf isotopic analyses were conducted using a Neptune Plus MC-ICP-MS equipped with a Geolas 2005 excimer ArF laser ablation system at the state Key Laboratory of Geological Processes and Mineral Resources, China University of Geosciences, Wuhan. All data were acquired on zircon in single spot ablation mode at a spot size of 44 μm in this study. Each measurement consisted of 20 s of acquisition of the background signal followed by 50 s of ablation signal acquisition. Detailed operating conditions for the laser ablation system and the analytical method are the same as description by Hu et al. [49]. The $^{176}Hf/^{177}Hf$ ratios of the standard zircon (GJ1) were 0.282013 ± 0.000022 (2σ, n=276), in agreement with recommended values within 2σ error [50,51]. Offline selection and integration of analyte signals, and mass bias calibrations were performed using ICPMSDataCal [46].

5.3. Whole-rock major and trace element analyses

Three fresh samples from the inner phase (SF-1 to SF-3) and three samples from the outer phase (SF-4 to SF-6) were collected for major and trace element determinations. Geochemical analyses were carried out at the Guangzhou Institute of Geochemistry, Chinese Academy of Sciences (GIG-CAS). Major element oxides were analyzed using a Rigaku RIX 2000 X-ray fluorescence spectrometer (XRF), and analytical uncertainties are mostly between 1 and 5% [52]. Trace elements were obtained by inductively coupled plasma-mass spectrometry (ICP-MS) after acid digestion of samples in high-pressure Teflon vessels, and detailed procedures are described by Li et al. [52]. The USGS and Chinese National standards AGV-2, GSR-1, GSR-2, MRG-1, BCR-1, W-2 and G-2 were chosen for calibrating element concentrations of the analyzed samples. Analytical precision of REE and other incompatible element analyses is typically 1-5%.

5.4. Fluid inclusion analysis

The fluid inclusion samples were collected from three mineralization stages, and then doubly polished into thin sections (<0.30mm thick) for petrographic study. The fluid inclusions were observed in the quartz (Figure 2), and we selected representative fluid inclusions to perform microthermometry and Raman microspectroscopy analysis at the state Key Laboratory of Geological Processes and Mineral Resources, China University of Geosciences, Wuhan. Microthermometric measurements were performed using a LINKAM THSMG600 heating and freezing stage with an operating range from −196 °C to +600 °C, equipped with an OLYMPUS 80 × ULWD objective. The heating and cooling rates were limited to less than 20 °C/min and reduced to 0.1–1 °C/min close to the phase change points. Melting temperatures of solid CO_2 ($T_{m,\ CO2}$), clathrate melting temperatures ($T_{m,\ cla}$), partial homogenization temperatures of CO_2 ($T_{h,\ CO2}$), ice melting temperatures ($T_{m,\ ice}$), halite dissolution temperatures ($T_{m,\ halite}$) and total homogenization temperatures (T_h) were measured. The salinities of inclusions were calculated using the final melting temperatures of CO_2 clathrates [53] and ice melting temperatures [54], respectively. Raman analysis was performed with a Renishaw MK1-1000 Raman microspectrometer by using a He-Ne laser with 514.5 nm excitation line and 2 to 4 mW at the sample. Integration time was 30 s, with five accumulations for each spectral line. The spectral resolution is ± 0.5 cm^{-1} with a beam size of 2 μm. The whole process was completed at room temperature (23 °C) and normal pressure.

6. Results

 doi:10.20944/preprints201811.0192.v1

6.1. Zircon U-Pb ages

The zircon U-Pb ages for 23 zircons are shown in Table 1. Most of the zircon grains from two samples (SF-1 and SF-5) are euhedral and prismatic, and are relatively transparent and colorless. They have a length between 61 μm and 179 μm, with length to width ratios between approximately 1:1–3:1 (Figure 6a, b). CL images show that most zircons have magmatic oscillatory overgrowth rims, although a few zircons with high uranium contents are dark brown and turbid (Figure 6a, b). Most zircons have high Th/U ratios >0.5, which are typical of an igneous origin. Twelve spot analyses of zircons from sample SF-1 yield $^{206}Pb/^{238}U$ ages of 297 Ma to 300 Ma (Figure 6c) with a weighted mean of 299 ± 1 Ma (MSWD = 1.04), and eleven spot analyses of zircons from sample SF-5 yield $^{206}Pb/^{238}U$ ages of 297 Ma to 300Ma (Figure 6d) with a weighted mean of 298 ± 1 Ma (MSWD = 1.3), which is interpreted as the magma crystallization age. The age of outer phase is coeval with the inner phase, indicating that the SAFG was formed in the Early Permian.

Table 1. Zircon LA-ICP-MS U–Pb data of the Shanshenfu alkali-feldspar granite.

Spot	Trace Elements (ppm)			Isotopic ratio						Apparent age (Ma)					
	U	Th	Th/U	$^{207}Pb/^{235}U$	1σ	$^{206}Pb/^{238}U$	1σ	$^{207}Pb/^{206}Pb$	1σ	$^{206}Pb/^{238}U$	1σ	$^{207}Pb/^{235}U$	1σ	$^{207}Pb/^{206}Pb$	1σ
Sample	SF-1														
SF1-1	635	337	0.53	0.3362	0.0039	0.0472	0.0002	0.0517	0.0006	297	1.7	294	4.0	272	21.3
SF1-2	591	349	0.59	0.3425	0.0046	0.0475	0.0002	0.0523	0.0007	299	1.9	299	4.6	298	-2.8
SF1-3	817	683	0.84	0.3341	0.0035	0.0473	0.0002	0.0512	0.0005	298	1.8	293	3.8	250	24.1
SF1-4	656	345	0.53	0.3413	0.0046	0.0475	0.0001	0.0521	0.0007	299	1.6	298	4.6	300	31.5
SF1-5	1413	809	0.57	0.3434	0.0024	0.0473	0.0001	0.0526	0.0004	298	1.6	300	3.0	322	14.8
SF1-6	495	262	0.53	0.3403	0.0052	0.0475	0.0002	0.0519	0.0008	299	1.8	297	5.1	283	30.6
SF1-7	1130	738	0.65	0.3468	0.0029	0.0476	0.0002	0.0528	0.0004	300	2.0	302	3.4	320	16.7
SF1-8	988	482	0.49	0.3463	0.0031	0.0476	0.0002	0.0528	0.0005	300	1.8	302	3.5	320	20.4
SF1-9	822	430	0.52	0.3465	0.0033	0.0476	0.0002	0.0528	0.0005	300	1.9	302	3.7	320	20.4
SF1-10	1202	673	0.56	0.3418	0.0024	0.0475	0.0002	0.0522	0.0004	299	2.0	299	3.0	295	14.8
SF1-11	191	144	0.76	0.3417	0.0124	0.0473	0.0002	0.0523	0.0019	298	2.0	298	11.1	298	79.6
SF1-12	719	283	0.39	0.3428	0.0046	0.0475	0.0002	0.0523	0.0007	299	1.8	299	4.6	298	-2.8
Sample	SF-5														
SF5-1	613	326	0.53	0.3459	0.0037	0.0476	0.0002	0.0527	0.0005	300	1.9	302	3.9	317	22.2
SF5-2	215	148	0.69	0.3457	0.0103	0.0475	0.0002	0.0527	0.0015	299	1.8	302	9.2	317	69.4
SF5-3	698	481	0.69	0.3456	0.0044	0.0475	0.0002	0.0528	0.0006	299	2.0	301	4.4	320	25.9
SF5-4	680	214	0.31	0.3413	0.004	0.0473	0.0001	0.0524	0.0006	298	1.6	298	4.1	302	25.9
SF5-5	1062	490	0.46	0.3397	0.0027	0.0475	0.0002	0.0519	0.0004	299	1.7	297	3.2	280	18.5
SF5-6	239	144	0.6	0.3451	0.0087	0.0475	0.0002	0.0526	0.0013	299	1.8	301	7.9	309	55.6
SF5-7	1077	67	0.06	0.3433	0.0025	0.0472	0.0001	0.0527	0.0004	298	1.6	300	3.1	317	23.1
SF5-8	201	95	0.47	0.3472	0.0142	0.0476	0.0001	0.0531	0.0022	300	1.7	303	12.5	332	92.6
SF5-9	1407	651	0.46	0.3501	0.0024	0.0472	0.0001	0.0538	0.0003	297	1.6	305	3.1	365	13.0
SF5-10	583	243	0.42	0.3407	0.0058	0.0472	0.0001	0.0523	0.0009	297	1.7	298	5.5	298	41.7
SF5-11	1213	646	0.53	0.3422	0.0027	0.0473	0.0001	0.0525	0.0004	298	1.6	299	3.2	306	12.0

Preprints (www.preprints.org) | NOT PEER-REVIEWED | Posted: 8 November 2018 doi:10.20944/preprints201811.0192.v1

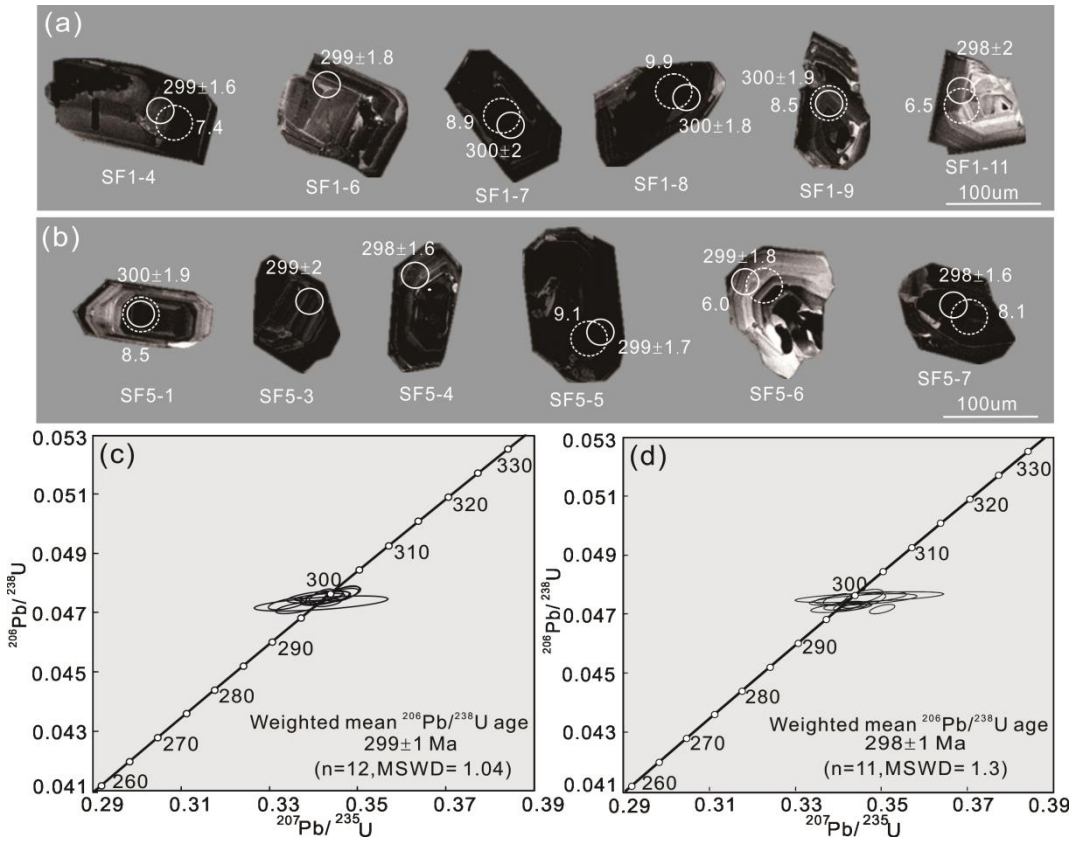

Figure 6. Zircon CL images and zircon U-Pb concordant curves for the inner phase (a, c) and outer phase (b, d) of the Shanshenfu alkali-feldspar granite.

6.2. Zircon trace element and Ti-in-zircon temperature

Trace element compositions of zircons are listed in Table 2, and the corresponding chondrite-normalized REE patterns are plotted in Figure 7. The zircons of sample SF-1 and SF-5 have ΣREE contents ranging from 3815 to 10727 ppm and 1411 to 8447 ppm, respectively, Ce anomalies ranging from 1.2 to 276 (average of 86) and 1.7 to 215 (average of 44), respectively, and Ti contents ranging from 8.6 to 58.3 ppm and 4.8 to 173 ppm, respectively. Most zircons have normal Ti values (≤75 ppm; [21]). Nonetheless, one grain of these analyzed zircons has yielded exceedingly high Ti value (SF5-9 = 173 ppm). Such surplus measured value cannot represent primary igneous zircon and may reflect inclusions (e.g. ilmenite) in zircon, and should be excluded from the following discussion. The temperature of the melt during zircon crystallization was calculated by the Ti-in-zircon thermometer [18] as shown in the following equations:

$$T_{zircon}(℃) = 4800 / (5.711 - \lg(Ti_{zircon}) - \lg(Si_a) + \lg(Ti_a)) - 273 \quad (1)$$

As quartz is one of the major mineral phases in the SAFG, the activity of silica (Si_a) is set to 1. Due to the absence of rutile in the SAFG, the activity of titanium (Ti_a) is conservatively estimated to be 0.6 [17,55]. The calculated Ti-in-zircon temperatures for the inner phase (sample SF-1) and the outer phase (sample SF-5) are in the range of 773 to 990 ℃ (average of 854 ℃) and 721 to 919 ℃ (average of 841 ℃) (Table 2), respectively.

Table 2. Zircon trace element abundance, Ce and Eu anomalies, Ti-in-zircon temperatures (T) and magmatic oxygen fugacity (fO_2) of the Shanshenfu alkali-feldspar granite.

spot	La ppm	Ce ppm	Pr ppm	Nd ppm	Sm ppm	Eu ppm	Gd ppm	Tb ppm	Dy ppm	Ho ppm	Er ppm	Tm ppm	Yb ppm	Lu ppm	ΣREE ppm	Ti ppm	δCe	δEu	T_{Ti} °C	lg(fO_2)	FMQ buffer	△FMQ
Sample SF-1																						
SF1-1	1.57	268	1.39	21.3	53.9	0.6	333	119	1451	510	2244	417	3937	663	10019	16.3	39.2	0.01	837	-10.1	-13.7	3.6
SF1-2	2.23	103	1.63	18.4	39.1	0.32	224	82.2	1050	395	1808	346	3297	566	7931	33.2	11.7	0.01	917	-11.5	-12.2	0.7
SF1-3	0.88	44.6	1.23	15.5	27.3	1.78	135	43.3	506	182	829	159	1586	284	3815	58.3	9.3	0.09	990	-9.9	-11.1	1.2
SF1-4	6.60	92.0	2.77	15.9	15.0	0.47	95.2	33.9	450	176	854	172	1798	321	4026	22.6	4.7	0.04	872	-16.7	-13.1	-3.6
SF1-5	0.11	161	0.74	19.8	58.6	0.26	348	126	1590	570	2490	457	4227	679	10727	19.1	120.8	0.01	854	-5.2	-13.4	8.2
SF1-6	210	750	84.6	433	154	2.44	280	67.4	674	217	934	179	1774	312	5861	24.6	1.2	0.04	882	-21.3	-12.9	-8.4
SF1-7	0.24	116	0.5	9.2	44.4	1.84	251	86.8	1097	385	1700	316	2933	475	7416	19.2	73.2	0.05	855	-7.0	-13.4	6.4
SF1-8	0.04	137	0.75	7.9	27.8	0.59	186	70.9	947	350	1602	306	2990	504	7130	8.6	174.8	0.03	773	-7.4	-15.1	7.7
SF1-9	0.49	152	1.45	14.3	27.2	0.61	163	59.1	757	281	1317	261	2633	443	6110	9.3	39.0	0.03	781	-12.6	-14.9	2.3
SF1-10	0.07	191	0.34	7.6	21.2	0.33	162	67.4	904	338	1576	297	2838	452	6855	13.9	270.5	0.02	820	-3.6	-14.1	10.5
SF1-11	5.14	147	2.31	18.6	33.7	0.28	208	81.2	1073	406	1859	362	3546	585	8322	16.7	9.2	0.01	840	-15.4	-13.7	-1.7
SF1-12	0.02	72.7	0.17	4.3	17.9	0.53	110	43.5	589	229	1105	224	2242	367	5005	14.2	276.0	0.04	823	-3.4	-14.0	10.6
Sample SF-5																						
SF5-1	3.49	99.6	2.87	32.7	42.1	1.53	198	60.2	707	237	1038	204	1995	334	4952	33.6	6.8	0.05	919	-13.5	-12.2	-1.3
SF5-2	0.50	184	0.49	9.6	30.9	0.11	180	69.9	936	358	1607	321	3265	500	7462	32.5	80.7	0.00	915	-4.3	-12.3	8.0
SF5-3	12.2	212	6.04	35.3	36.1	0.24	199	75.3	987	369	1676	336	3362	528	7822	12.1	5.3	0.01	807	-18.9	-14.4	-4.5
SF5-4	5.38	183	2.59	22.3	36.9	0.49	232	92.7	1142	382	1685	338	3349	488	7954	9.2	10.6	0.02	780	-17.6	-14.9	-2.7
SF5-5	0.16	135	0.11	6.7	20.7	0.51	168	63.6	876	320	1488	290	2977	431	6777	20.4	215.0	0.03	861	-2.7	-13.3	10.6
SF5-6	0.31	161	1.34	17.9	38.1	0.27	216	76.6	962	347	1561	320	3247	502	7450	18.9	53.8	0.01	853	-8.3	-13.4	5.1
SF5-7	57.0	260	19.2	84.4	38.8	1.45	171	57.9	748	271	1258	255	2667	409	6241	9.8	1.7	0.05	786	-24.2	-14.8	-9.4
SF5-8	1.14	156	0.83	13.9	30.1	0.69	188	74.1	970	357	1595	324	3276	473	7459	18.4	34.8	0.03	850	-10.0	-13.5	3.5
SF5-9	0.36	87.4	0.42	6.8	15.1	0.27	82.6	27.8	370	134	627	135	1424	225	3135	173	48.3	0.02	1158	-	-	-
SF5-10	0.20	20.0	0.35	3.4	6.19	1.98	42.1	13.2	160	60.9	285	59.2	651	107	1410	33.5	16.4	0.38	918	-10.2	-12.2	2.0
SF5-11	4.03	109	1.65	14.6	30.1	0.78	204	78.5	1068	403	1890	376	3683	585	8444	4.8	9.2	0.03	721	-21.0	-16.3	-4.7

Note: T_{Ti} (°C) is the Ti temperature of zircon, $\delta Ce=Ce_N/(La_N\times Pr_N)^{0.5}$, $\delta Eu=Eu_N/(Sm_N\times Gd_N)^{0.5}$; FMQ buffer is the buffer of the fayalite-magnetite-quartz, which is calculated using the formula FMQ buffer =−24441.9/(T+273)+8.290 (±0.167) [56]; △FMQ=lgfO_2-FMQ buffer.

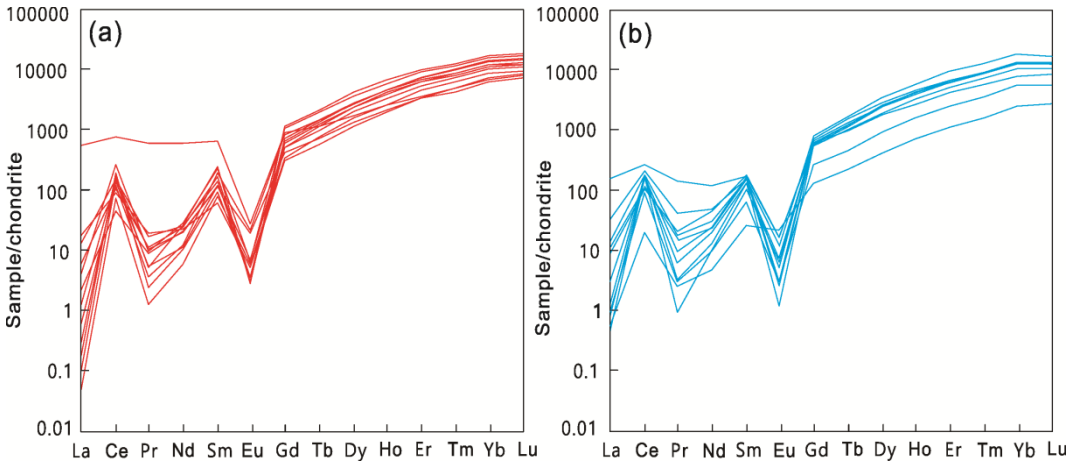

Figure 7. Chondrite-normalized REE patterns for the zircons from the Shanshenfu alkali-feldspar granite. (a) The inner phase; (b) The outer phase. Normalization values for chondrite are from McDonough and Sun [57].

6.3. Zircon Lu–Hf isotopes

The analytical results on Hf isotopes for zircons are listed in Table 3. The $\varepsilon_{Hf}(t)$ values are calculated using their U-Pb ages. Seven spots from the inner phase show a range of initial $^{176}Hf/^{177}Hf$ ratios from 0.282955 to 0.283052 and $\varepsilon_{Hf}(t)$ values from +6.5 to +9.9, with the two-stage Hf model ages (T_{DM2}) from 394 to 587 Ma. Nine spots from the outer phase show a range of initial $^{176}Hf/^{177}Hf$ ratios from 0.282941 to 0.283029 and $\varepsilon_{Hf}(t)$ values from +6.0 to +9.1, with T_{DM2} from 441 to 614 Ma.

Table 3. LA-MC-ICP-MS zircon Lu-Hf isotope data for the Shanshenfu alkali-feldspar granite.

Spot	$^{176}Hf/^{177}Hf$[a]	1σ	$^{176}Lu/^{177}Hf$[a]	1σ	$^{176}Yb/^{177}Hf$[a]	1σ	Age (Ma)	$\varepsilon_{Hf}(t)$[b]	1σ	T_{DM1} (Ma)[c]	T_{DM2} (Ma)[d]	$f_{Lu/Hf}$
Sample SF-1												
SF1-1	0.282995	0.000015	0.002996	0.000008	0.086319	0.000235	297	7.9	0.74	384	507	-0.91
SF1-4	0.282982	0.000014	0.002209	0.000051	0.061855	0.001585	299	7.4	0.70	395	533	-0.93
SF1-7	0.283024	0.000015	0.004243	0.000064	0.115732	0.00164	300	8.9	0.75	353	450	-0.87
SF1-8	0.283052	0.000016	0.003983	0.000026	0.117902	0.00081	300	9.9	0.76	307	394	-0.88
SF1-9	0.283011	0.000014	0.003086	0.000051	0.089502	0.001556	300	8.4	0.72	362	476	-0.91
SF1-11	0.282955	0.000013	0.00128	0.000005	0.032593	0.000132	298	6.5	0.70	424	587	-0.96
SF1-12	0.282967	0.000014	0.002444	0.000009	0.068065	0.000324	299	6.9	0.73	420	563	-0.93
Sample SF-5												
SF5-1	0.283011	0.000017	0.004065	0.000056	0.11864	0.001618	300	8.4	0.79	372	476	-0.88
SF5-2	0.283020	0.000014	0.002091	0.000018	0.055445	0.0004	299	8.8	0.72	338	458	-0.94
SF5-5	0.283029	0.000017	0.003066	0.000016	0.090641	0.000562	299	9.1	0.79	335	441	-0.91
SF5-6	0.282941	0.000014	0.000794	0.000014	0.020234	0.000404	299	6.0	0.70	438	614	-0.98
SF5-7	0.283002	0.000014	0.003232	0.000016	0.093923	0.000628	298	8.1	0.72	377	494	-0.90
SF5-8	0.282948	0.000015	0.001153	0.000078	0.029802	0.002258	300	6.2	0.73	433	602	-0.97
SF5-9	0.283015	0.000014	0.003446	0.00001	0.099972	0.000247	297	8.6	0.72	359	468	-0.90
SF5-10	0.283025	0.000014	0.002295	0.000037	0.066671	0.001076	297	8.9	0.72	333	448	-0.93
SF5-11	0.283028	0.000015	0.003929	0.00002	0.113707	0.000769	298	9.0	0.75	344	443	-0.88

[a] The measured values.

[b] Initial $^{176}Hf/^{177}Hf$ ratios were calculated using the measured $^{176}Lu/^{177}Hf$ ratios and the ^{176}Lu decay constant of 1.867×10^{-11} yr^{-1} [58], and ε_{Hf} values were calculated using the chondritic ratios of $^{176}Hf/^{177}Hf$ (=0.282772) and $^{176}Lu/^{177}Hf$ (=0.0332) [59].

[c] The single-stage model age (T_{DM1}) was calculated using the present-day ratios $^{176}Hf/^{177}Hf$=0.28325 and $^{176}Lu/^{177}Hf$=0.0384 [60].

[d] Two-stage model age (T_{DM2}) was calculated by projecting the initial $^{176}Hf/^{177}Hf$ ratios of the zircon back to the depleted mantle model growth curve, assuming a $^{176}Lu/^{177}Hf$ value of 0.015 for the average continent crust [61].

6.4. Whole-rock major and trace element analyses

The major- and trace-element compositions of the SAFG are shown in Table 4 as weight percent (wt.%) for major oxides and as parts per million (ppm) for all trace elements. All samples are characterized by high SiO_2 (74.89–76.83 wt.%), Al_2O_3 (12.34–12.85 wt.%), and alkali (Na_2O+K_2O = 8.17–8.81 wt.%) and low MgO (0.09–0.16 wt.%) and CaO (0.08–0.24 wt.%). They exhibit a high-K calc-alkaline, peraluminous and high-differentiation, with A/CNK (molar Al_2O_3/CaO+Na_2O+K_2O) ranging from 1.04 to 1.12 and A/NK (molar Al_2O_3/ Na_2O+ K_2O) from 1.06 to 1.14 (Figure 8a and b). Samples exhibit enriched REEs (except Eu) with total REE ranging from 147 to 357 ppm. They are characterized by slightly enriched light REE (LREE) ($(La/Yb)_N$ = 2.02–6.57) and flat heavy REE (HREE) ($(Gd/Yb)_N$ = 0.6–1.27) with strong negative Eu anomalies (δEu = 0.05–0.12） (Figure 8d). All samples are enriched in large-ion lithophile elements (LILEs) (e.g. Rb, Th, U and K), high-field-strength elements (HFSEs) (e.g. Nb, Ta, Zr and Hf), and exhibit strong depletion of Ba, Sr, P and Ti (Figure 8c).

Table 4. Major oxides and trace elements of the Shanshenfu alkali-feldspar granite.

Sample	The inner phase			The outer phase		
	SF-1	SF-2	SF-3	SF-4	SF-5	SF-6
SiO_2	76.83	75.23	76.02	76.22	74.89	75.36
Al_2O_3	12.34	12.56	12.78	12.67	12.85	12.54
Fe_2O_3	1.51	1.48	1.37	1.64	2.13	1.95
CaO	0.08	0.11	0.09	0.19	0.21	0.24
MgO	0.14	0.12	0.11	0.16	0.09	0.12
Na_2O	3.71	4.08	3.87	3.67	4.23	4.13
K_2O	4.46	4.31	4.42	4.87	4.53	4.68
TiO_2	0.15	0.27	0.19	0.17	0.25	0.31
MnO	0.06	0.08	0.04	0.11	0.05	0.06
P_2O_5	0.03	0.08	0.04	0.06	0.11	0.08
LOI	0.45	0.67	0.54	0.24	0.48	0.37
Total	99.98	99.56	99.71	100.32	99.67	99.48
La	52.3	22.6	45.5	58.8	27.2	40.1
Ce	161	54.2	101.3	174.5	72.3	89.6
Pr	14.75	6.58	13.2	15.1	7.22	12.6
Nd	53.6	20.8	44.2	51.3	29.1	45.5
Sm	12.8	5.13	9.35	11.26	7.32	9.81
Eu	0.34	0.15	0.13	0.42	0.17	0.21
Gd	10.72	5.82	7.62	10.11	9.61	6.97
Tb	1.91	1.28	1.18	1.83	2.36	1.11
Dy	12.3	10.44	7.61	12.28	13.12	6.5
Ho	2.54	2.35	1.51	2.57	2.68	1.27
Er	8.57	7.42	4.83	7.93	6.68	5.24
Tm	1.25	1.11	0.68	1.17	0.97	0.72
Yb	8.65	8.03	4.97	8.21	7.32	5.16
Lu	1.4	1.28	0.83	1.32	1.15	0.88
Ga	21.2	19.7	22.6	24.3	21.8	18.9

Preprints (www.preprints.org) | NOT PEER-REVIEWED | Posted: 8 November 2018 doi:10.20944/preprints201811.0192.v1

Rb	177	153.5	172	181.5	167	148
Ba	60.2	107	171	58.6	123	86
Th	16.3	17.51	14.2	17.1	18.2	13.6
U	3.79	3.65	3.48	2.87	3.67	3.13
Ta	2.23	2.65	2.31	2.95	2.46	2.33
Nb	43.7	49.1	44.3	48.2	46.2	44.7
Sr	8.3	14.8	22.4	24.1	15.3	18.7
Zr	358	435	647	248	487	276
Hf	11.9	13.1	18.4	10.8	13.9	11.2
Y	70.4	75.1	81.8	54.2	78.3	63.1
ΣREE	342	147	243	357	187	226
δEu	0.09	0.08	0.05	0.12	0.06	0.08

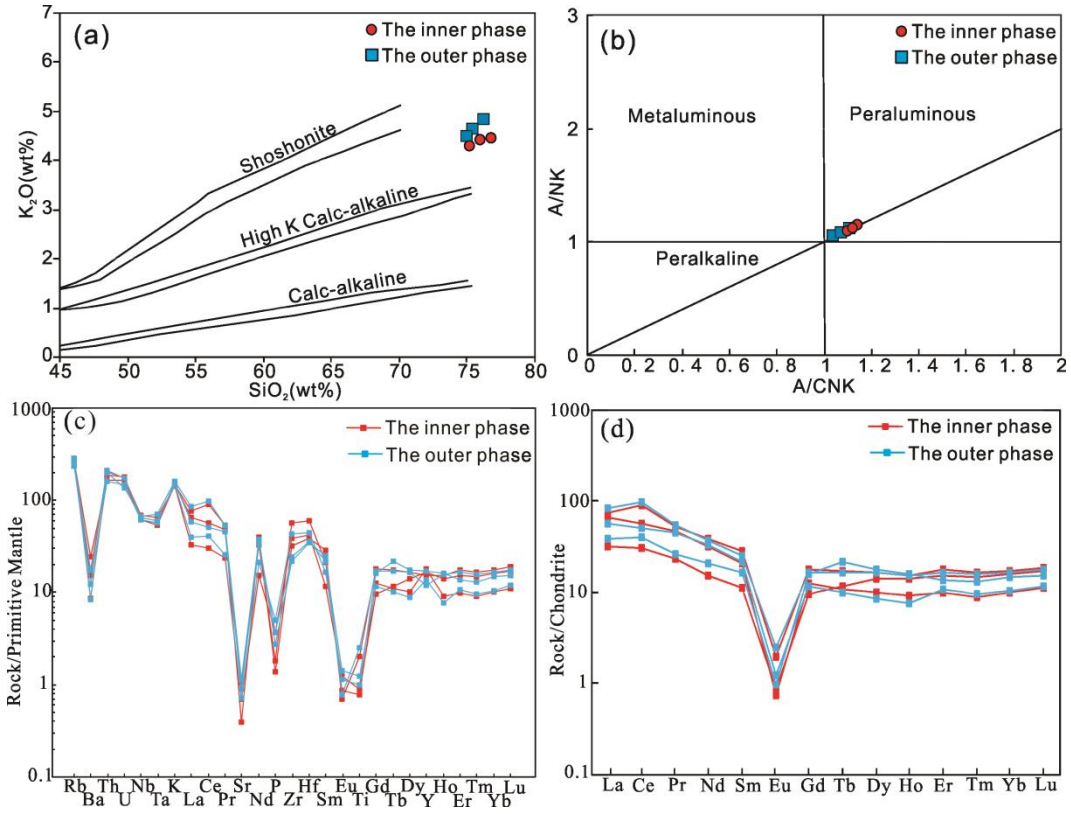

Figure 8. (a) SiO_2 vs. K_2O diagram of the Shanshenfu alkali-feldspar granite. (after Peccerillo and Taylor, 1976); (b) A/NK vs. A/CNK diagram, where A/NK = $Al_2O_3/(Na_2O+K_2O)$ and A/CNK = $Al_2O_3/(CaO+Na_2O+K_2O)$ (all oxides on molar basis); (c) Primitive mantle-normalized trace element diagram; (d) Chondrite-normalized REE pattern. Normalization values are from Sun and McDonough [62].

6.5. Fluid inclusion

6.5.1. Fluid inclusion petrography

Only primary fluid inclusions (FIs) occur as random groups or isolated individuals were analyzed in the quartz crystals of each mineralization stage in the Hongyan Cu-polymetallic deposit. Four major types of FIs are identified based on their nature of phase relationships at room (21 °C) temperatures, phase transformation during cooling and heating processes, and laser Raman spectroscopy analysis (Figure 9): daughter mineral-bearing CO_2 inclusions (SC-type), CO_2-H_2O

 doi:10.20944/preprints201811.0192.v1

inclusions (C-type), daughter mineral-bearing aqueous inclusions (SW-type) and two-phase aqueous inclusions (W-type). SC-type FIs occur in four phases (S_{Halite}+V_{CO2}+L_{CO2}+L_{H2O}) CO_2-H_2O-NaCl systems at room temperature (Figure 9a). They only occur as isolated individuals in the stage I K-feldspar–quartz–pyrite vein. They are negative-crystal or irregular in shape with sizes of 8–16um. The CO_2 phase accounts for 20–35% of the total volume. C-type FIs occur in three phases (V_{CO2}+L_{CO2}+L_{H2O}) CO_2–H_2O–NaCl system at room temperature (Figure 9b–e). They generally occur as random groups or isolated individuals in stage I and II quartz veins. They are negative-crystal, elliptical or irregular in shape with sizes of 8–15um. The CO_2 phase accounts for 25–40% of the total volume. SW-type FIs occur in three phases (S_{Halite} + V_{H2O} + L_{H2O}) CO_2–H_2O–NaCl systems at room temperature (Figure 9f, g). They generally occur as isolated individuals in stage I and II quartz veins. They are irregular or elliptical in shape with sizes of 6–20um. The vapor phase accounts for 10–40% of the total volume. W-type FIs occur in two phases (V_{H2O} + L_{H2O}) or a single aqueous phase at room temperature (Figure 9), and are widely developed in each mineralization stage. They are negative-crystal, elliptical or irregular in shape with sizes of 4–22um. The vapor phase accounts for 10–85% of the total volume.

The relative abundances of FIs were investigated for quartz in each mineralization stage. The stage I quartz veins contained large amounts of C- and W-types, followed by S-type and a few SC-type FIs. The stage II quartz veins contained abundant C- and W-types FIs and a few S-type FIs without SC-type FIs. The stage III quartz veins only contained W-type FIs. The above results indicate that the CO_2 content of fluids decreased from the early stage to late stage.

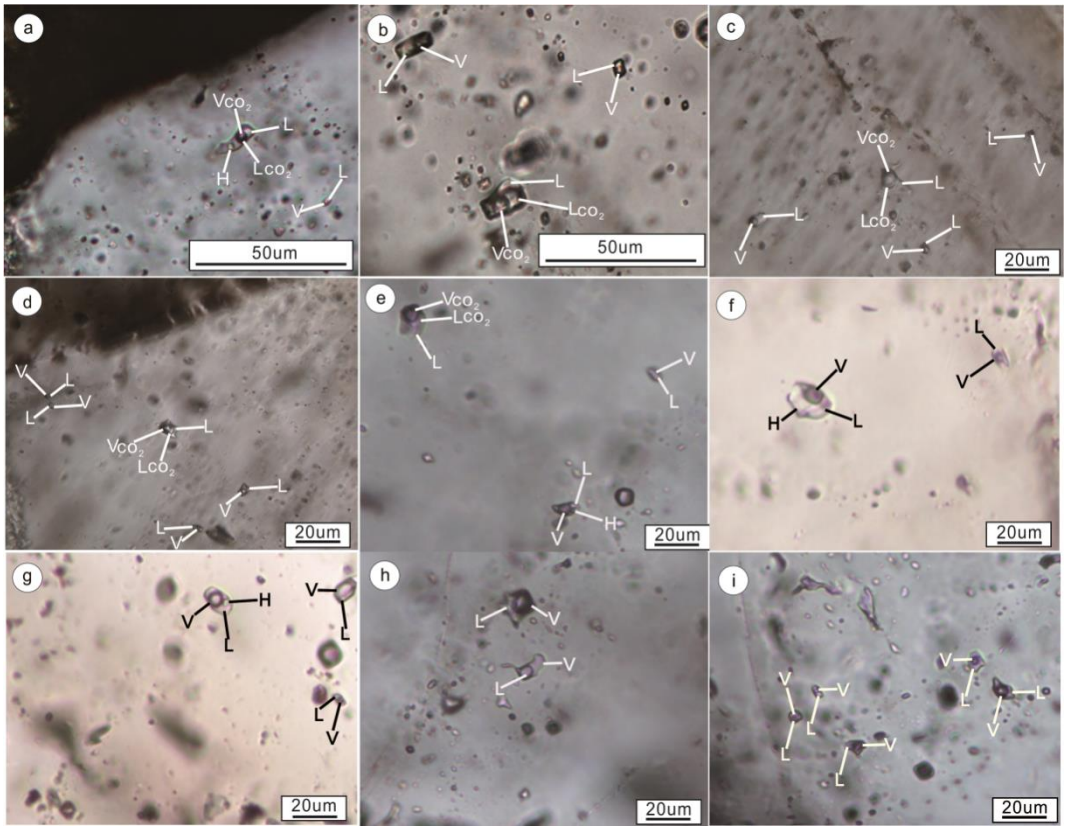

Figure 9. Photomicrographs of fluid inclusions in the Hongyan Cu-polymetallic deposit: (a) the SC-type and W-type inclusions in the stage I; (b-c) the C-type and W-type inclusions in the stage I; (d) the C-type and W-type inclusions in the stage II; (e) the coexisting C-type and SW-type inclusions in the stage II; (f) the S-type and W-type inclusions in the stage I; (g) the S-type and W-type inclusions in

Preprints (www.preprints.org) | NOT PEER-REVIEWED | Posted: 8 November 2018 doi:10.20944/preprints201811.0192.v1

the stage II; (h-i) the W-type inclusions in the stage III. Abbreviation: L-liquid; V-vapor; V_{CO_2}-CO_2 vapor; L_{CO_2}-CO_2 liquid; H-halite.

6.5.2. Raman analysis

Phases in representative fluid inclusions were measured using Laser Raman microspectroscopy to constrain their compositions. The vapor bubbles of the SC-type FIs in quartz of stage I are dominated by CO_2 (1277 cm-1, 1379 cm-1) and SO_2 (1150 cm-1) (Figure 10a). The vapor bubbles of the C-type FIs in quartz of stage II are dominated by CO_2 (1276 cm-1, 1379 cm-1) and H_2O (Figure 10b).

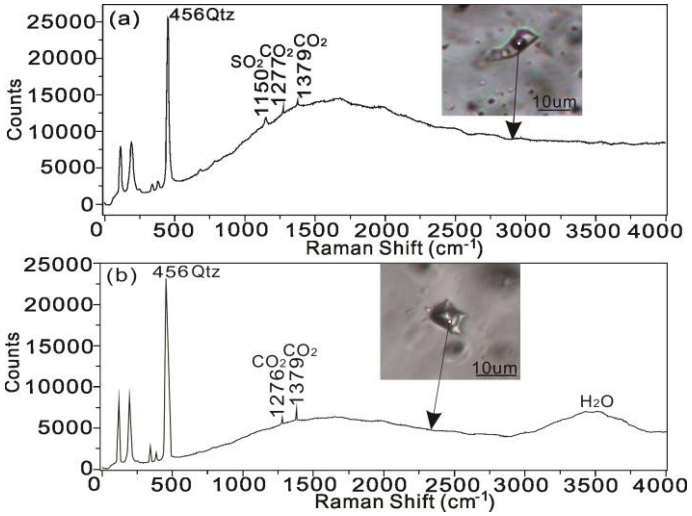

Figure 10. Laser-Raman spectrum of fluid inclusions in the Hongyan Cu-polymetallic deposit: (a) Spectrum for vapor bubbles of the SC-type inclusion in the stage I; (b) Spectrum for vapor bubbles of the C-type inclusion in the stage II.

6.5.3. Microthermometry

Microthermometric results of the studied fluid inclusions from three mineralization stages are summarized in Table 5 and graphically illustrated in Figure 11.

Table 5. Microthermometric data of fluid inclusions of the Hongyan Cu-polymetallic deposit.

Stage	Host mineral	Type	N	Size (um)	$T_{m, CO2}$ (℃)	$T_{m, ice}$ (℃)	$T_{m, cla}$ (℃)	$T_{h, CO2}$ (℃)	$T_{m, halite}$ (℃)	T_h (℃)	Salinity(wt.% NaCl)
I	Quartz	C	15	10 ~ 15	-57.6 ~ -56.4		1.8 ~ 8.3	24.3 ~ 29.8		321 ~ 413	3.3 ~13.5
		SC	6	8 ~ 16	-61.2 ~ -56.4		3.5 ~ 7.8	26.2 ~ 31.1		353 ~ 402	4.3 ~ 11.2
		SW	11	8 ~ 20					302 ~ 456	302 ~ 456	38.3 ~ 54.0
		W	25	5 ~ 16		-15.1 ~ -2.5				287 ~ 492	4.2 ~ 18.7
II	Quartz	C	10	8 ~ 15	-57.8 ~ -56.6		3.7 ~ 8.9	23.9 ~ 29.3		254 ~ 375	2.2 ~ 10.9
		SW	8	6 ~ 14					175 ~ 287	258 ~ 356	30.7 ~ 43.9
		W	24	6 ~ 22		-10.4 ~ -1.5				241 ~ 385	2.6 ~ 14.4
III	Quartz	W	28	4 ~ 13		-6.1 ~ -0.7				165 ~ 294	1.2 ~ 9.3

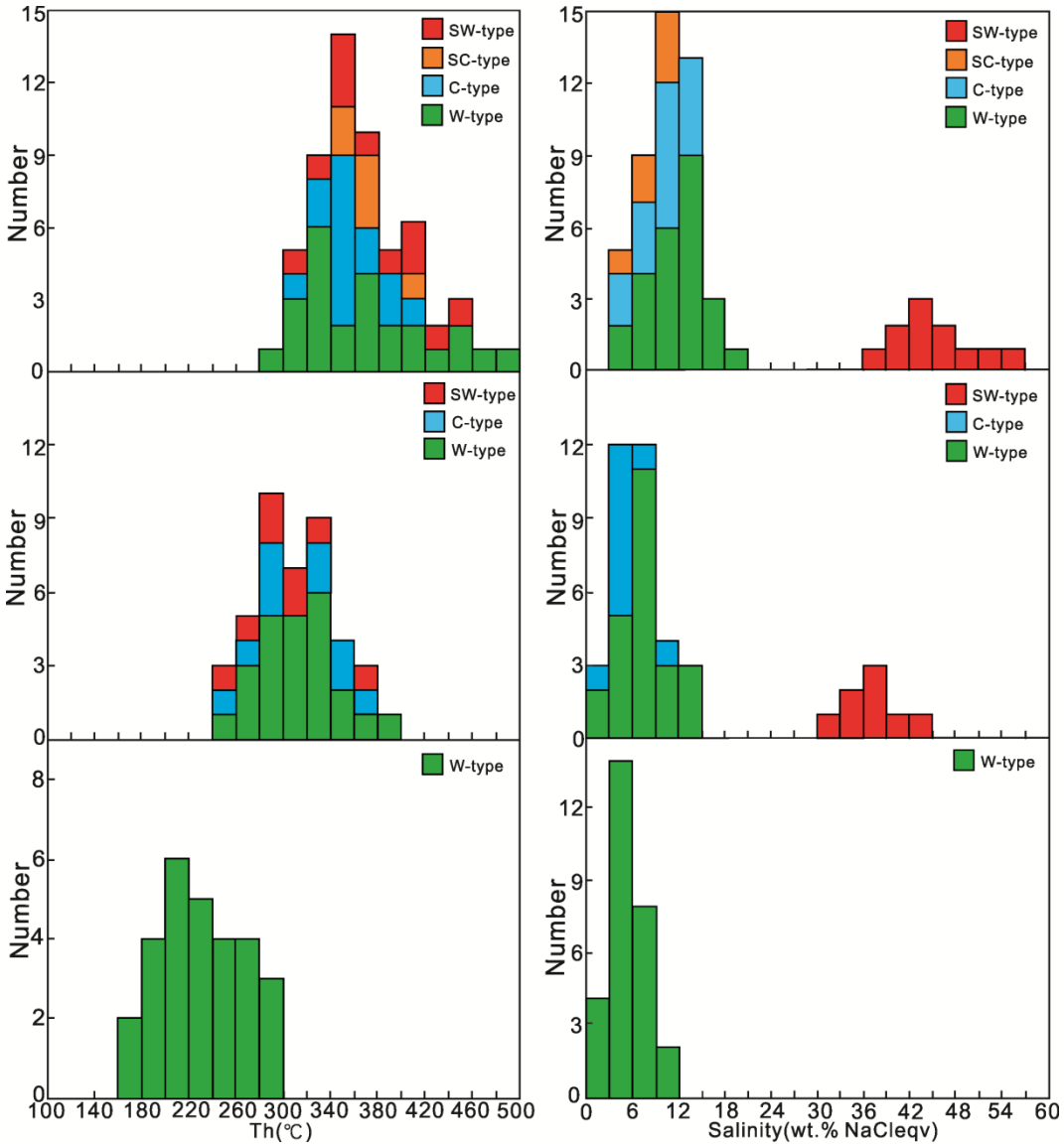

Figure 11. Histograms of homogenization temperatures and salinities of fluid inclusions of the Hongyan Cu-polymetallic deposit.

In stage I quartz veins, the C-type FIs have CO_2 phases of 25–80% in volume (Figure 9b, c), and yield melting temperature of solid CO_2 ($T_{m,CO2}$) of −57.6 to −56.4 °C, suggesting the purity of the CO_2 phase. The clathrate melting temperatures ($T_{m,cla}$) occur in the interval of 1.8–8.3°C, corresponding to salinities of 3.3–13.5 wt% NaCl eqv. They mostly homogenize to liquid at temperatures of 321–413 °C, with CO_2 phases partially homogenizing to liquid or vapor at temperatures of 24.3–29.8 °C. The SC-type FIs contain halite daughter minerals (Figure 9a) that do not melt in the heating processes. They have vapor CO_2 phases of 20–40% in volume, and their $T_{m,CO2}$ range from −61.2 to −56.4 °C, suggesting the presence of a small amount of other gases in the CO_2 phase [63]. Their $T_{m,cla}$ occur in the interval of 3.5–7.8°C, corresponding to salinities of 4.3–11.2 wt% NaCl eqv. They mostly homogenize to liquid at temperatures of 353–402 °C, with CO_2 phases partially homogenizing to liquid or vapor, or by critical behavior at temperatures of 26.2–31.1 °C. The SW-type FIs have vapor bubbles of 15–60% in volume (Figure 9f), and mostly homogenize to liquid at temperatures of 302–456 °C. The halite dissolution temperatures ($T_{m,halite}$) vary from 302 to 456 °C, corresponding to

Preprints (www.preprints.org) | NOT PEER-REVIEWED | Posted: 8 November 2018 doi:10.20944/preprints201811.0192.v1

salinities of 38.3–54.0 wt% NaCl eqv. The W-type FIs have vapor bubbles of 10–75% in volume, and homogenize to liquid or vapor at temperatures between 287 and 492 °C with yielding ice melting temperatures ($T_{m,ice}$) from −15.1 to −2.5 °C, corresponding to salinities of 4.2–18.7 wt% NaCl eqv.

In stage II quartz veins, the C-type FIs have CO_2 phases of 35–85% in volume (Figure 9d, e), and yield $T_{m,CO2}$ of −57.8 to −56.6 °C, suggesting the purity of the CO_2 phase. Their $T_{m,cla}$ occur in the interval of 3.7–8.9 °C, corresponding to salinities of 2.2–10.9 wt% NaCl eqv. They homogenize to liquid or vapor at temperatures between 254 and 375 °C. Their CO_2 phases partially homogenize to liquid or vapor at temperatures ($T_{h,CO2}$) between 23.9 and 29.3 °C. The SW-type FIs have vapor bubbles of 25–75% in volume (Figure 9e, g), and homogenize to liquid or vapor at temperatures of 258–356 °C. Their $T_{m,halite}$ vary from 175 to 287 °C, corresponding to salinities of 30.7–43.9 wt% NaCl eqv. The W-type FIs have vapor bubbles of 10–90% in volume (Figure 9d, e, g), and homogenize to liquid or vapor at temperatures between 241 and 385 °C with yielding $T_{m,ice}$ from −10.4 to −1.5 °C, corresponding to salinities of 2.6–14.4 wt% NaCl eqv.

In stage III quartz veins, the W-type FIs have vapor bubbles of 15–85% in volume (Figure 9h, i), and homogenize to liquid or vapor at temperatures between 165 and 294 °C with yielding $T_{m,ice}$ from −6.1 to −0.7 °C, corresponding to salinities of 1.2–9.3 wt% NaCl eqv.

7. Discussion

7.1. Magmatic oxygen fugacity, petrogenesis and implications for mineralization

The SAFG has high SiO_2 (74.89–76.83 wt.%), total alkalis ($K_2O + Na_2O$ = 8.17–8.81 wt.%) and low P_2O_5 (0.03–0.11 wt.%) contents (Table 4). It also has enriched HFSE (e.g. Nb, Ta, Zr and Hf) and REEs (except Eu), and obviously depleted Si, Ba, P, Ti and Eu (Figure 8c and d). These features indicate that the SAFG is a typical A-type granite [4]. This is also supported by the evidence that all the samples fall into A-type field on the discrimination diagrams of Whalen et al. [64] (Figure 12a) and plot in the within-plate-granite field on the diagram Y vs. Nb of Pearce et al. [65] (Figure 12b). Chondrite normalized REE patterns of the studied zircons show that they are depleted in LREE and enriched in HREE, and exhibit strong positive Ce anomalies (δCe = 1.22–275.99) and deep negative Eu anomalies (δEu = 0.1–0.38) (Figure 7), which are typical of unaltered magmatic zircons [21]. Positive Ce anomalies may be related to a relatively oxidized melt with favorable incorporation of Ce^{4+} while negative Eu anomalies may be resulted from plagioclase fractionation in magma composition [19,20]. Due to the close relationship between the Ce anomaly in zircon and the oxidation state of the melt from which the zircon crystallizes [19,20], zircon becomes a powerful indicator for the fO_2 of magmas. A new calibration has been presented by Trail et al. [19,20] to determine the oxygen fugacity of magmatic melt based on the incorporation of cerium into zircon and Ti-in-zircon temperature, which can be expressed by the following empirical equation:

$$\ln\left(\frac{Ce}{Ce^*}\right)_D = (0.1156 \pm 0.0050) \times \ln(fO_2) + \frac{13860 \pm 708}{T(K)} - 6.125 \pm 0.484 \quad (1)$$

where fO_2 represents oxygen fugacity, and T is absolute temperature calculated by revised Ti-in-zircon thermometry. The Ce anomaly can be estimated by the following equation:

$$\left(\frac{Ce}{Ce^*}\right)_D \approx \left(\frac{Ce}{Ce^*}\right)_{CHUR} = \frac{Ce_N}{\sqrt{La_N \cdot Pr_N}} \quad (2)$$

where Ce_N, La_N, and Pr_N are chondrite-normalized values for Ce, La, and Pr in zircon, respectively.

Preprints (www.preprints.org) | NOT PEER-REVIEWED | Posted: 8 November 2018 doi:10.20944/preprints201811.0192.v1

The lgfO$_2$ values for the zircons of the inner phase and the outer phase are in the range of −21.3 to −3.4 (average of −10.3) and −24.2 to −2.7 (average of −13.1), respectively, with corresponding ΔFMQ values of −8.4 to +10.6 (average of +3.1) and −9.4 to +10.6 (average of +0.7), respectively (Table 2). By plotting the Ti-in-zircon temperatures and their logarithmic oxygen fugacities on T vs lg(fO$_2$) diagram (Figure 12c) that can be divided by the curves of some specific mineral oxidation buffers such as magnetite-hematite (MH), fayalite-magnetite-quartz (FMQ), and iron-wustite (IW) into several oxygen fugacity fields [19], the data points of most zircons mainly fall beyond FMQ buffer (Figure 12c). The difference in the oxygen fugacity of both magmatic phases can be well explained by Oppenheimer et al. [66] that it is more favorable for the closed-system magma to preserve the deep oxidized signatures, suggesting that the parental magma of the SAFG has higher oxygen fugacity than that of the inner phase.

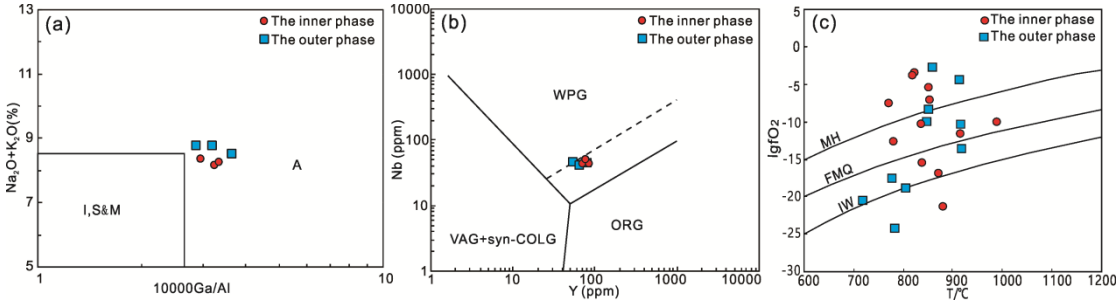

Figure 12. (a) K$_2$O+Na$_2$O vs. 10000 Ga/Al discrimination diagram of Whalen et al. [64], I, S and M=I-, S-and M-type granites; (b) Y vs. Nb tectonic discrimination diagram of Pearce et al. [65]. VAG=volcanic arc granites, WPG=within plate granites, COLG=collisional granites, ORG=oceanic ridge granites; (c) Magmatic oxygen fugacity (fO$_2$) of the Shanshenfu alkali-feldspar granite.

Numerous studies suggest that the high magmatic oxygen fugacity is closely related to the nature of magma source regions [14,29,67]. Several petrogenetic models have been proposed for the origin of A-type granites, including (1) extreme fractional crystallization of mantle-derived tholeiitic or alkaline basaltic magma progenitors [6,68]; (2) low-degree partial melting of lower-crustal granulites with depletion of incompatible elements [69]; (3) anatexis of underplated I-type tonalitic crustal source [11,70,71]; and (4) hybridization between anatectic crustal and mantle-derived magmas, such as crustal assimilation and fractional crystallization of mantle-derived magmas, or of mixing between mantle-derived and crustal magmas [11,71,72]. The zircons of the SAFG exhibit high $\varepsilon_{Hf}(t)$ values (+ 6.0 to + 9.9) and young T_{DM2} (394 to 614 Ma) (Table 3), which is consistent with juvenile crustal sources. Thus, we can rule out the possibility of partial melting of lower-crustal granulites. The Ti-in-zircon temperatures of the SAFG can reach 721–990 °C, which reveals that the anatexis of underplated I-type tonalitic crust is unlikely to be the source because it cannot provide such high melting temperature for the formation of A-type granites [6,73,74]. Thus, extreme fractional crystallization from mantle-derived basaltic magma or hybridization between anatectic crustal and mantle-derived magmas may be the possible source and requires further discussion.

The SAFG not only has similar U-Pb age and $\varepsilon_{Hf}(t)$ values to Late Carboniferous arc intrusions from the northern Inner Mongolia (Figure 13a, b), but also has the high oxygen fugacity similar to those of arc magmas that can range from FMQ to FMQ+6 [67]. The reason for the high oxygen fugacity of arc magmas is that the melted upper oceanic slab can make sulfur mainly in the form of sulfate and SO$_2$ dissolved in magma (approximately 1.5%, [75]) and then deliver these volatile substances to the mantle wedge through the dehydration of oceanic slab [46]. Two discrimination

Preprints (www.preprints.org) | NOT PEER-REVIEWED | Posted: 8 November 2018 doi:10.20944/preprints201811.0192.v1

diagrams based on U/Yb ratio vs. Y and Hf content were proposed by Grimes et al. [24] to distinguish between zircons from continental crust, ocean crust, and the mantle (kimberlite megacrysts). In Figure 13c and d, most of the studied zircons plot in the field of ocean crust zircon and intesection field between continental zircon and ocean crust zircon. The evidences above suggust that arc-related juvenile crust may be an effective source of the SAFG. Although this magma source of A-type granites has been proposed by many previous studies [76–78], the nature of the magma source is controversial. Due to the absence of spatial and coeval associated alkaline mafic magmatism in the study area, alkali basaltic juvenile crust is not a suitable source for the SAFG. By contrast, the coexist of the Early Permian A- and I-type granites commonly occurs along the HHSZ [77,78]. Zhang et al. [77] and Yuan et al. [79] proposed that the Early Permian I-type granites near the central HHSZ were generated by partial melting of mantle-derived basaltic juvenile crust, whereas the coeval A-type granites originated from remelting of charnockitized juvenile crust. This interpretation has also been recognized by previous studies [80,81]. Therefore, the SAFG may be derived from the crustal assimilation and fractional crystallization of the charnockitized juvenile crust. Based on related studies conducted on hydrothermal deposits, the arc-related juvenile crust source and high magmatic oxygen fugacity of the SAFG are the two key factors resulting in hydrothermal mineralization: On the one hand, the magma source of the SAFG can supply enough H_2O, SO_2, CO_2, and metals into the magma systems [27,28]; On the other hand, high magmatic oxygen fugacity of SAFG favors transmission of the chalcophile elements (e.g., Cu, Au, Ag) of the source region into the melt together with oxidized sulfur, rather than into the sulfides (reduced sulfur) [14,29,39], then these metal elements will be enriched in the fluid phases after magmatic fractional crystallization, consequently facilitating subsequent hydrothermal mineralization.

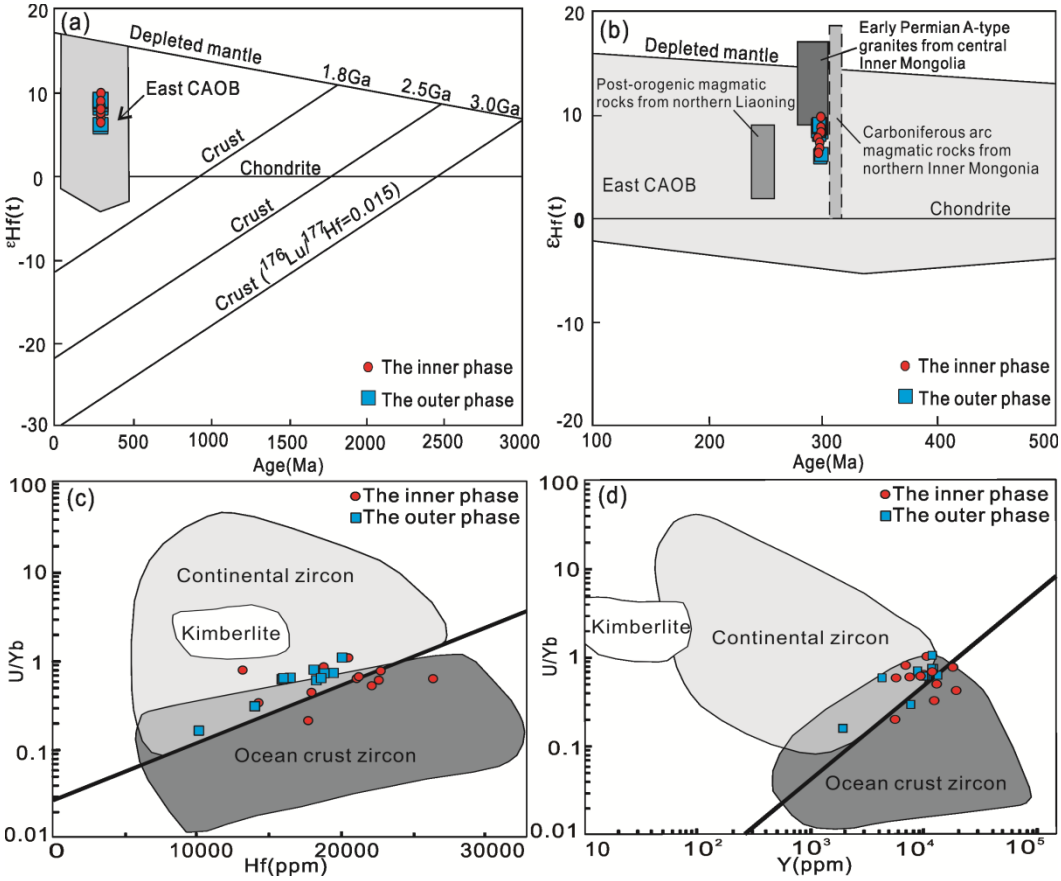

 doi:10.20944/preprints201811.0192.v1

Figure 13. (a, b) Compilation diagram of ε_{Hf} (t) vs U-Pb age of the Shanshenfu alkali-feldspar granite. The Hf isotopic evolution line of the Archean average crust with $^{176}Lu/^{177}Hf = 0.015$ is after Griffin et al. [60]. The fields for Carboniferous arc intrusions from northern Inner Mongolia, Early Permian A-type granites from central Inner Mongolia and Late Permian to Early Triassic post-orogenic melts from northern Liaoning are from Chen et al. [37], Zhang et al. [77] and Zhang et al. [82], respectively. (c, d) U/Yb ratio vs. Y and Hf content diagrams of Grimes et al. [24] to discriminate between continental and oceanic crust zircon. Heavy lines indicate the lower limit of zircons from continental crust.

7.2. The origin and evolution of ore-forming fluids

At the Hongyan Cu-polymetallic deposit, various types of FIs including SC-, SW-, C- and W-type FIs can be observed in hydrothermal quartz. The distribution, homogenization temperatures and salinities of these FIs in each mineralization stage provide invaluable information on the nature and evolution of the ore-forming fluids. All these types of FIs can be observed in the stage I quartz, which suggests that these fluids belong to an H_2O–CO_2–NaCl system. These FIs yield high homogenization temperatures of 287 to 492 °C and high salinities of 38.3 to 54.0 wt% NaCl eqv (Table 5). The presence of SC- and C-type FIs reveals considerable amounts of CO_2 in the stage I (Figure 9a–c). The occurrence of magnetite in the quartz−K-feldspar veins (Figure 4e) suggest high fO_2 in this stage [14,19], which is further evidenced by the presence of SO_2 in the CO_2 phase of the SC-type FIs (Figure 10a). In conclusion, the fluids of the stage I are characterized by high temperature, high salinity, CO_2-rich and relatively oxidizing. The above features suggest that the fluids in the stage I exsolved from granitic magmatism [83]. Apparently, the SAFG transferred large amounts of SO_2, CO_2 and metals into the early hydrothermal systems (Stage I) by magmatic fractional crystallization [27,28,39]. The precipitation of minor magnetite in the stage I generally facilitates the subsequent precipitation of ore-forming fluids [29]: The decrease of Fe^{3+} content in the fluids caused the conversion of oxidized sulfur to reduced sulfur, which led to the initial precipitation of metal elements due to the decrease of fO_2. However, most of the sulfur within the stage I was present as oxidized sulfur due to the high oxygen fugacity, which led to the occurrence of minimal mineralization in this stage. The homogenization temperatures (241–385 °C) and salinities (2.2–43.9 wt% NaCl eqv) of FIs in the stage II are obviously lower than those of the stage I (Figure 11), which suggests that the hydrothermal system is cooled down due to mixtures of magmatic and meteoric fluids. Moreover, the coexistence of high salinity S-type FIs and low salinity C-type FIs can be observed in this stage (Figure 9e), and their homogenization temperatures are similar, which indicate intensive fluid immiscibility or boiling corresponding to the decrease of pressure and temperature. Fluid immiscibility results in a loss of volatile such as CO_2 and SO_2 [84,85], which is evidenced by the disappearance of SC-type FIs in the stage II quartz veins. Such degassing of oxidized gas increases the reducibility of the ore-forming fluids, which is considered as a key process responsible for sulfide precipitation [14]. The superposition of multiple factors including the hydrothermal fluid cooling, fluid immiscibility, CO_2 escape and decrease of fO_2 is the key cause of sulfide precipitation and intense Cu-Au mineralization in the stage II quartz–polymetallic sulfide veins. With the addition of large volumes of meteoric water, the CO_2 content, temperature and salinity of hydrothermal fluids dramatically decreased, consequently the stage III quartz contains only low homogenization temperatures (164–294 °C) and salinities (1.2–9.3 wt% NaCl eqv) of W-type FIs (Table 5), and the effects of primary magmatic fluids can be ignored. The barren mineralization in this stage are resulted from consumption of most metal elements in the earlier

stage and the addition of large volumes of meteoric water. Accordingly, the petrological, microthermometric and laser Raman microspectroscopic results above indicate that the fluid system changed from the initial high temperature, high salinity, high fO_2 and CO_2-rich magmatic-hydrothermal fluids of stage I to CO_2-poor, dilute, and cooling meteoric fluids of stage III.

7.3. Geodynamic implication

It has been recognized that A-type granites can be formed in a variety of extensional regimes, such as continental back-arc extension, post-collisional extension or within-plate settings [2,86]. Eby [2] divided the A-type granites into A1 and A2 groups. The A1 group is emplaced in anorogenic settings such as plumes, hotspots or continental rift zones. The A2 group is related to a cycle of subduction-zone or continent-continent collision magmatism in crust and emplaced in a variety of tectonic settings. In our study, all granite samples of the SAFG mainly fall in the A2 field on the Nb-Y-3Ga diagram of Eby [2] (Figure 14a), and plot in the post-orogenic extension setting on the R2 versus R1 diagram of Batchelor and Bowden [87] (Figure 14b), which suggests that the SAFG seems to form in a similar post-orogenic extension setting to the coeval counterparts along the HHSZ during the Permian [4,77,88]. The latest research suggests that the emplacement of the Hegenshan ophiolite should have happened before the Early Permian, most likely between 300 Ma and 335 Ma [89,90]. Meanwhile, the Permian and Carboniferous submarine turbidite strata with predominant magmatic arc source exsists along the HHSZ [91]. This suggests that the ocean along the Hegenshan-Heihe was closed during the Late Carboniferous. However, the last Paleo-Asian ocean was not closed along the HHSZ during the Late Carboniferous but closed along the Solonker-Xra Moron-Changchun suture during the Late Permian–Early Triassic [92]. This is well evidenced by Late Permian to Early Triassic post-orogenic magmatic rocks form belts along the Solonker-Xra Moron-Changchun suture [11,72]. The SAFG together with the other Permian A2-type granites [3,4,7–10] are commonly coexistence with the Carboniferous calc-alkaline I-type magmatism along the HHSZ [37]. The increase in granitoid alkalinity with time indicates the tectonic transition from an earlier arc setting to a later extensional setting [93]. Taking into account the fact that the Permian A2-type granites (260–300 Ma) are strikingly sparse and small in volume, and show a NE-trending migration together with the widespread occurrence of Permian volcanic rocks of island arc affinity and Late Permian terrestrial sediments along the HHSZ [4], we propose the post-collisional slab break-off process along the HHSZ during the Permian [71,94] that not only terminates a prolonged northward subduction of the Paleo-Asian ocean, but also heralds the amalgamation between the Songliao terrane and the Liaoyuan terrane along the Ondor Temple-Xar Moron suture zone. Meanwhile, Such tectonic setting is also compatible with the high temperature, high salinity, CO_2-rich, and relatively oxidizing magmatic fluids in the Hongyan Cu-polymetallic deposit [83,95]. The age of mineralized A-type granite in the Hongyan Cu-polymetallic deposit is consistent with the mineralized A-type granites in the southwestern part of the HHSZ [10], which suggests that these A-type granites associated with mineralization are formed in the same extension setting. During the Permian, the HHSZ was characterized by post-collisional extensional tectonism with the slab break-off, which not only causes upwelling of asthenospheric mantle and result in partial melting of the overlying lithospheric mantle and the juvenile arc crust [77], but also provides the thermal flux to form some narrow extensional magmatic passages, subsequently followed by A-type magmatism with mineralization potential along the HHSZ. Thus, the Permian A-type granites with arc-related

juvenile crustal source and high fO_2 along the HHSZ have great potential for prospecting related hydrothermal deposits, and need more attention in future exploration.

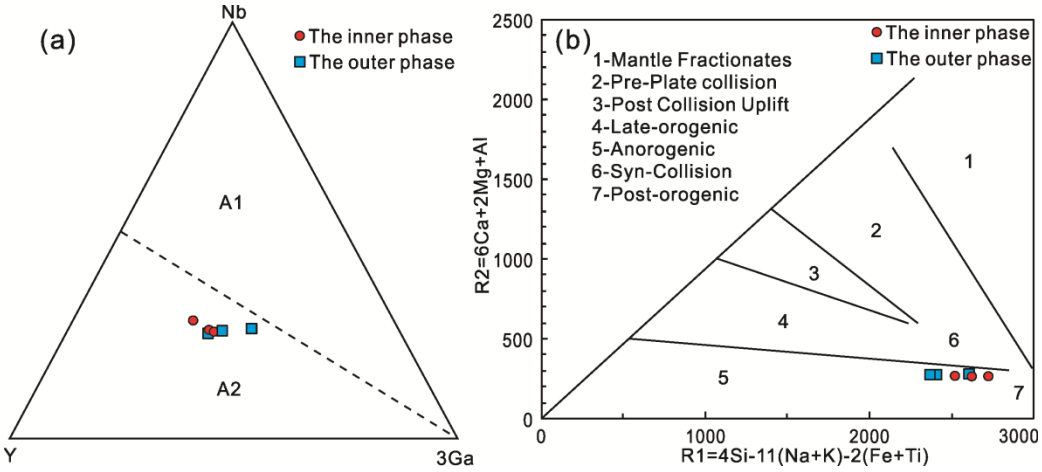

Figure 14. (a) Nb-Y-Ga ternary diagram of Eby [2]; (b) R2 (=6Ca+2Mg+Al) vs. R1 (=4Si–11(Na+K)–2(Fe+Ti)) diagram of Batchelor and Bowden [87].

8. Conclusions

Based upon geochronological, geochemical and fluid inclusion studies in the Hongyan Cu-polymetallic deposit, the following conclusions can be drawn:

(1) LA-ICP-MS U-Pb zircon dating shows that the inner phase and outer phase of the SAFG was formed at 299 ± 1 Ma and 298± 1 Ma, respectively, which indicates that the SAFG was formed in the Early Permian.

(2) The SAFG is a typical A-type granite with high magmatic oxygen fugacity that may be derived from the crustal assimilation and fractional crystallization of the charnockitized juvenile crust.

(3) The early ore-forming fluids (stage I) in the Hongyan Cu-polymetallic deposit are the initial high temperature, high salinity, high fO_2 and CO_2-rich magmatic-hydrothermal fluids derived from magmatic fractional crystallization of the SAFG, and then evolved into the later CO_2-poor, dilute, and cooling meteoric fluids (stage III).

(4) Combined with regional geological background, we propose that the SAFG was formed in post-collisional extensional tectonism with the slab break-off. In future exploration for prospecting hydrothermal deposits along the HHSZ, the Permian A-type granites with arc-related juvenile crustal source and high fO_2 have great potential and need more attention.

Author Contributions: Data curation, C.M.; Formal analysis, C.M.; Funding acquisition, X.L.; Investigation, C.M., X.L. and C.C.; Project administration, X.L. and C.C.; Writing – original draft, C.M.; Writing – review & editing, C.M., X.L. and C.C.

Funding: This research was supported by the Geological Survey Project of China Geological Survey Bureau (NMKD2010-3).

Acknowledgments: We gratefully thank Hu Qingcheng and Yang Yongsheng from Institute of Geological Survey, China University of Geosciences, Wuhan, for their important guidance and assistance in microthermometry and Raman microspectroscopy analysis.

Conflicts of Interest: The authors declare no conflict of interest.

References

1. Loiselle, M.C.; Wones, D.R. Characteristics and origin of anorogenic granites. *Geol. Soc. Am. Abstr. Prog.*

1979, *11*, 468.

2. Eby, G.N. Chemical subdivision of the A-type granitoids: petrogenetic and tectonic implications. *Geology* **1992**, *20*, 641–644, https://doi.org/10.1130/0091-7613 (1992)020<0641:CSOTAT>2.3.CO;2.
3. Hong, D.W.; Huang, H.Z.; Xiao, Y.J.; Xu, H.M. Permian alkaline granites in center Inner Mongolia and their geodynamic significance. *Acta Geol. Sin.* **1994**, *68*, 219–230, (In Chinese) DOI:10.3321/j.issn:0001-5717.1994.03.001.
4. Wu, F.Y.; Sun, D.Y.; Li, H.M.; Jahn, B.M.; Wilde, S. A-type granites in northeastern China: age and geochemical constraints on their petrogenesis. *Chem. Geol.* **2002**, *187*, 143–173, https://doi.org/10.1016/S0009-2541(02)00018-9.
5. Wu, S.P.; Wang, M.Y.; Qi, K.J. Present situation of researches on A-type granites: a review. *Acta Petrol. Mineral.* **2007**, *26*, 57–66, (In Chinese with English abstract) DOI:10.3969/j.issn.1000-6524.2007.01.009.
6. Bonin, B. A-type granites and related rocks: Evolution of a concept, problems and deposits. *Lithos* **2007**, *97*, 1–29, https://doi.org/10.1016/j.lithos.2006.12.007.
7. Shi, G.H.; Miao, L.C.; Zhang, F.Q.; Jian, P.; Fan, W.M.; Liu, D.Y. The age and its district tectonic implications on the Xilinhaote A-type granites, Inner Mongolia. *Chinese Sci. Bull.* **2004**, *49*, 384–389, (In Chinese) DOI:10.3321/j.issn:0023- 074X.2004.04.015.
8. Zhang, Y.Q.; Xu, L.Q.; Kang, X.L. Age dating of alkali granite in Jingesitai area of Dong Ujingqin Banner, Inner Mongolia, and its significance. *Geol. Chin.* **2009**, *36*, 988–995, (In Chinese) DOI:10.3969/j.issn.1000-3657.2009.05.004
9. Guo, K.C.; Zhang, W.L.; Yang, X.P.; Wang, L.; Shi, D.Y.; Yu, H.T.; Su, H. Origin of early Permian A-type granite in the Wudaogou area, Heihe City. *J. Jilin Univ. (Earth Sci. Ed.)* **2011**, *41*, 1077–1083, (In Chinese with English abstract). DOI: 10.13278/j.cnki.jjuese.2011.04.038.
10. Yang, K. Ore-forming Characters and Depositing Orientation of Metal Deposit in the Dong Ujimqin, Inner Mongolia. Master Thesis, China University of Geosciences in Wuhan, Wuhan, China, 2013.
11. Dall'Agnol, R.; Oliveira, D.C. Oxidized, magnetite-series, rapakivi-type granites of Carajás, Brazil: implications for classification and petrogenesis of A-type granites. *Lithos* **2007**, *93*, 215–233, https://doi.org/10.1016/j.lithos.2006.03.
12. Han, Y.G.; Zhang, S.H.; Pirajno, F.; Zhou, X.W.; Zhao, G.C.; Qu, W.J.; Liu, S.H.; Zhang, J.M.; Liang, H.B.; Yang, K. U-Pb and Re-Os isotopic systematics and zircon Ce^{4+}/Ce^{3+} ratios in the Shiyaogou Mo deposit in eastern Qinling, central China: Insights into the oxidation state of granitoids and Mo (Au) mineralization. *Ore Geol. Rev.* **2013**, *55*, 29–47, https://doi.org/10.1016/j.oregeorev.2013.04.006.
13. Qiu, J.T.; Yu, X.Q.; Santosh, M.; Zhang, D.H.; Chen, S.Q.; Li, J.P. Geochronology and magmatic oxygen fugacity of the Tongcun molybdenum deposit, northwest Zhejiang, SE China. *Miner. Depos.* **2013**, *48*, 545–556, https://doi.org/10.1007/s00126-013-0456-5.
14. Sun, W.D.; Huang, R.F.; Li, H.; Hu, Y.B.; Zhang, C.C.; Sun, S.J.; Zhang, L.P.; Ding, X.; Li, C.Y.; Zartman, R.E. Porphyry deposits and oxidized magmas. *Ore Geol. Rev.* **2015**, *65*, 97–131, https://doi.org/10.1016/j.oregeorev.2014.09.004.
15. Cisse, M.; Lü, X.B.; Algeo, T.J.; Cao, X.F.; Li, H.; Wei, M.; Yuan, Q.; Chen, M. Geochronology and geochemical characteristics of the Dongping ore-bearing granite, North China: Sources and implications for its tectonic setting. *Ore Geol. Rev.* **2017**, *89*, 1091–1106. https://doi.org/10.1016/j.oregeorev.2016.07.006.
16. Wang, X.D.; Xu, D.M.; Lv, X.B.; Wei, W.; Mei, W.; Fan, X.J.; Sun, B.K. Origin of the Haobugao skarn Fe-Zn polymetallic deposit, Southern Great Xing'an range, NE China: Geochronological, geochemical, and Sr-Nd-Pb isotopic constraints. *Ore Geol. Rev.* **2018**, *94*, 58–72, https://doi.org/10.1016/j.oregeorev.2018.01.022.

17. Watson, E.B.; Wark, D.A.; Thomas, J.B. Crystallization thermometers for zircon and rutile. Contrib. *Mineral. Petrol.* **2006**, *151*, 413–433, https://doi.org/10.1007/ s00410-006-0068-5.
18. Ferry, J.M.; Waston, E.B. New thermodynamic models and revised calibrations for the Ti-in-zircon and Zr-in-rutile thermometers. Contrib. *Mineral. Petrol.* **2007**, *154*, 429–437, https://doi.org/10.1007/s00410-007-0201-0.
19. Trail, D.; Watson, E.B.; Tailby, N.D. The oxidation state of Hadean magmas and implications for early Earth's atmosphere. *Nature* **2011**, *480*, 79–82, https://doi.org/10.1038/nature10655.
20. Trail, D.; Watson, E.B.; Tailby, N.D. Ce and Eu anomales in zircon as proxies for oxidation state of magmas. *Geochim. Cosmochim. Acta* **2012**, *97*, 70–87, https://doi.org/10.1016/j.gca.2012.08.032.
21. Hoskin, P.W.O.; Schaltegger, U. The composition of zircon and igneous and metamorphic petrogenesis. *Rev. Mineral. Geochem.* **2003**, *53*, 27–62, https://doi.org/10.2113/0530027.
22. Hanchar, J.M.; VanWestrenen, W. Rare earth element behavior in zircon-melt systems. *Elements* **2007**, *3*, 37–42, https://doi.org/10.2113/gselements.3.1.37.
23. Hoskin, P.W.O. Trace-element composition of hydrothermal zircon and the alteration of Hadean zircon from the Jack Hills, Australia. *Geochim. Cosmochim. Acta* **2005**, *69*, 637–648, https://doi.org/10.1016/j.gca.2004.07.006.
24. Grimes, C.B.; John, B.E.; Kelemen, P.B.; Mazdab, F.K.; Wooden, J.L.; Cheadle, M.J.; Hanghøj, K.; Schwartz, J.J. Trace element chemistry of zircons from oceanic crust: a method for distinguishing detrital zircon provenance. *Geology* **2007**, *35*, 643–646, https://doi.org/10.1130/G23603A.1.
25. Yang, J.H.; Wu, F.Y.; Wilde, S.A.; Xie, L.W.; Yang, Y.H.; Liu, X.M. Tracing magma mixing in granite genesis: in situ U–Pb dating and Hf-isotope analysis of zircons. *Contrib. Mineral. Petrol.* **2007**, *153*, 177–190, http://dx.doi.org/10.1007/s00410-006-0139-7.
26. Cherniak, D.J.; Watson, E.B. Diffusion in zircon. *Rev. Mineral. Geochem.* **2003**, *53*, 113–143, https://doi.org/10.2113/0530113.
27. Maughan, D.T.; Keith, J.D.; Christiansen, E.H.; Pulsipher, T.; Hattori, K.; Evans, N.J. Contributions from mafic alkaline magmas to the Bingham porphyry Cu-Au-Mo deposit, Utah, USA. *Min. Depos.* **2002**, *37*, 14–37, DOI: 10.1007/s00126-001-0228-5.
28. Ma, X.H.; Chen, B.; Yang, M.C. Magma mixing origin for the Aolunhua porphyry related to Mo-Cu mineralization, eastern Central Asian Orogenic belt. *Gondwana Res.* **2013**, *24*, 1152–1171, http://dx.doi.org/10.1016/j.gr.2013.02.010.
29. Sun, W.D.; Liang, H.Y.; Ling, M.X.; Zhan, M.Z.; Ding, X.; Zhang, H.; Yang, X.Y.; Li, Y.L.; Ireland, T.R.; Wei, Q.R.; Fan, W.M. The link between reduced porphyry copper deposits and oxidized magmas. *Geochim. Cosmochim. Acta* **2013**, *103*, 263–275, https://doi.org/10.1016/j.gca.2012.10.054.
30. Lu, Y.J.; Loucks, R.R.; Fiorentini, M.L.; McCuaig, T.C.; Evans, N.J.; Yang, Z.M.; Hou, Z.Q.; Kirkland, C.L.; Parra-Avila, L.A.; Kobussen, A. Zircon compositions as a pathfinder for porphyry Cu ± Mo ± Au deposits. Soc. Econ. *Geol. Spec. Publ.* **2016**, *19*, 329–347.
31. Klemm, L.M.; Pettke, T.; Heinrich, C.A. Fluid and source magma evolution of the Questa porphyry Mo deposit, New Mexico, USA. *Miner. Depos.* **2008**, *43*, 533–552, DOI: 10.1007/s00126-008-0181-7.
32. Fan, H.R.; Hu, F.F.; Wilde, S.A.; Yang, K.F.; Jin, C.W. The Qiyugou gold-bearing breccia pipes, Xiong'ershan region, central China: fluid inclusion and stable-isotope evidence for an origin from magmatic fluids. *Int. Geol. Rev.* **2011**, *53*, 25–45, http//dx.doi.org/10.1080/00206810902875370.
33. Qiu, K.F.; Marsh, E.; Yu, H.C.; Pfaff, K.; Gulbransen, C.; Gou, Z.Y.; Li, N. Fluid and metal sources of the Wenquan porphyry molybdenum deposit, Western Qinling, NW China. Ore Geol. Rev. **2017**, 86, 459–473,

https://doi.org/10.1016/j.oregeorev.2017.02.035.

34. Mao, J.W.; Pirajno, F.; Cook, N. Mesozoic metallogeny in East China and corresponding geodynamic settings—An introduction to the special issue. *Ore Geol. Rev.* **2011**, *43*, 1–7, https://doi.org/10.1016/j.oregeorev.2011.09.003.
35. Wu, F.Y.; Sun, D.Y.; Ge, W.C.; Zhang, Y.B.; Grant, M.L.; Wilde, S.A.; Jahn, B.M. Geochronology of the Phanerozoic granitoids in northeastern China. *J. Asian Earth Sci.* **2011**, *41*, 1–30, https://doi.org/10.1016/j.jseaes.2010.11.014.
36. Gao, S.; Xu, H.; Zang, Y.; Wang, T. Mineralogy, ore-forming fluids and geochronology of the Shangmachang and Beidagou gold deposits, Heilongjiang province, NE China. *J. Geochem. Explor.* **2018**, *188*, 137–155, https://doi.org/10.1016/j.gexplo.2017.12.016.
37. Chen, B.; Jahn, B.M.; Tian, W. Evolution of the Solonker suture zone: constraints from zircon U-Pb ages, Hf isotopic ratios and whole-rock Nd–Sr isotope compositions of subduction and collision-related magmas and forearc sediments. *J. Asian Earth Sci.* **2009**, *34*, 245–257, https://doi.org/10.1016/j. jseaes.2008.05.007.
38. Zhang, X.H.; Xue, F.H.; Yuan, L.L.; Wilde, S.A. Late Permian appinite–granite complex from northwestern Liaoning, North China craton: petrogenesis and tectonic implications. *Lithos* **2012**, *155*, 201–217, https://doi.org/10.1016/j.lithos.2012.09.002.
39. Wang, Y.H.; Zhao, C.B.; Zhang, F.F.; Liu, J.J.; Wang, J.P.; Peng, R.M.; Liu, B. SIMS zircon U-Pb and molybdenite Re-Os geochronology, Hf isotope, and whole-rock geochemistry of the Wunugetushan porphyry Cu-Mo deposit and granitoids in NE China and their geological significance. *Gondwana Res.* **2015**, *28*, 1228–1245, https://doi.org/10.1016/j.gr.2014.10.001.
40. Zhou, Z.H.; Mao, J.W.; Wu, X.L.; Ouyang, H.G. Geochronology and geochemistry constraints of the Early Cretaceous Taibudai porphyry Cu deposit, northeast China, and its tectonic significance. *J. Asian Earth Sci.* **2015**, *103*, 212–228, https://doi.org/10.1016/j.jseaes.2014.06.013.
41. Liu, W.; Liu, X.J.; Liu, L.Q. Underplating generated A- and I-type granitoids of the East Junggar from the lower and the upper oceanic crust with mixing of mafic magma: insights from integrated zircon U-Pb ages, pertrography, geochemistry and Nd-Sr-Hf isotopes. *Lithos* **2013**, *179*, 293–319, https://doi.org/10.1016/j.lithos.2013.08.009.
42. Mao, J.W.; Wang, Y.T.; Zhang, Z.H.; Yu, J.J.; Niu, B.G. Geodynamic settings of Mesozoic large-scale mineralization in North China adjacent areas. *Sci. Chin. Ser. D* **2003**, *46*, 838–851, https://doi.org/10.1007/BF02879527.
43. Zhang, F.F.; Wang, Y.H.; Liu, J.J.; Wang, J.P.; Zhao, C.B.; Song, Z.W. Origin of the Wunugetushan porphyry Cu–Mo deposit, Inner Mongolia, NE China: constraints from geology, geochronology, geochemistry, and isotopic compositions. *J. Asian Earth Sci.* **2016**, *117*, 208–224, https://doi.org/10.1016/j.jseaes.2015.12.018.
44. Zeng, Q.D.; Liu, J.M.; Zhang, L.C. Re-Os geochronology of porphyry molybdenum deposit in southern segment of Da Hinggan Mountains, Northeast China. *J. Earth Sci.* **2010**, *21*, 390–401, https://doi.org/10.1007/s12583-010-0102-4.
45. Liu, Y.S.; Hu, Z.C.; Gao, S.; Günther, D.; Xu, J.; Gao, C.G.; Chen, H.H. In situ analysis of major and trace elements of anhydrous minerals by LA-ICP-MS without applying at internal standard. *Chem. Geol.* **2008**, *257*, 34–43, https://doi.org/10.1016/j.chemgeo.2008.08.004.
46. Liu, Y.S.; Gao, S.; Hu, Z.C.; Gao, C.G.; Zong, K.Q.; Wang, D.B. Continental and oceanic crust recycling-induced melt-peridotite interactions in the Trans-North China Orogen: U-Pb dating, Hf isotopes and trace elements in zircons of mantle xenoliths. *J. Petrol.* **2010**, *51*, 537–571, https://doi.org/10.1093/petrology/egp082.

47. Ludwig, K.R. Isoplot 3.00. A Geochronological Toolkit for Microsoft Excel. Berkeley Geochronol. *Center Spec. Publ.* **2003**, *No. 4*.
48. Qiu, J.T.; Song, W.J.; Jiang, C.X.; Wu, H.; Dong, R.M. CGDK: an extensible CorelDRAW VBA program for geological drafting. *Computers Geosci.* **2013**, *51*, 34–48, https://doi.org/10.1016/j.cageo.2012.07.020.
49. Hu, Z.C.; Liu, Y.S.; Gao, S.; Liu, W.G.; Yang, L.; Zhang, W.; Tong, X. R.; Lin, L.; Zong, K.Q.; Li, M.; Chen, H.H.; Zhou, L.; Yang, L. Improved in situ Hf isotope ratio analysis of zircon using newly designed X skimmer cone and Jet sample cone in combination with the addition of nitrogen by laser ablation multiple collector ICP-MS. *J. Anal. At. Spectrom.* **2012**, *27*, 1391–1399, https://doi.org/10.1039/c2ja30078h.
50. Woodhead, J.; Herget, J.; Shelley, M.; Eggins, S.; Kemp, R. Zircon Hf-isotope analysis with an excimer laser, depth profiling, ablation of complex geometries, and concomitant age estimation. *Chem. Geol.* **2004**, *209*, 121–135, https://doi.org/10.1016/j.chemgeo.2004.04.026.
51. Wu, F.Y.; Yang, Y.H.; Xie, L.W.; Yang, J.H.; Xu, P. Hf isotopic compositions of the standard zircons and baddeleyites used in U-Pb geochronology. *Chem. Geol.* **2006**, *234*, 105–126, https://doi.org/10.1016/j.chemgeo.2006.05.003.
52. Li, X.H.; Li, Z.X.; Wingate, M.T.D.; Chung, S.L.; Liu, Y.; Lin, G.C.; Li, W.X. Geochemistry of the 755Ma Mundine Well dyke swarm, northwestern Australia: part of a Neoproterozoic mantle superplume beneath Rodinia? *Precambr. Res.* **2006**, *146*, 1–15, https://doi.org/10.1016/j.precamres.2005.12.007.
53. Collins, P.L.F. Gas hydrates in CO_2-bearing fluid inclusions and the use of freezing data for estimation of salinity. *Econ. Geol.* **1979**, *74*, 1435–1444, http://dx.doi.org/10.2113/gsecongeo.74.6.1435.
54. Bodnar, R.J. Revised equation and table for determining the freezing point depression of H_2O-NaCl solutions. *Geochim. Cosmochim. Acta* **1993**, *57*, 683–684, https://doi.org/10.1016/0016-7037(93)90378-A.
55. Hiess, J.; Nutman, A.P.; Bennett, V.C.; Holden, P. Ti-in-zircon thermometry applied to contrasting Archean metamorphic and igneous systems. *Chem. Geol.* **2008**, *247*, 323–338, https://doi.org/10.1016/j.chemgeo.2007.10.012.
56. Myers, J.; Eugster, H.P. The system Fe-Si-O: Oxygen buffer calibrations to 1500K. *Contrib. Mineral. Petrol.* **1983**, *82*, 75–90.
57. McDonough, W.F.; Sun, S.S. The composition of the Earth. Chem. Geol. **1995**, 120, 223–253, https://doi.org/10.1016/0009-2541(94)00140-4.
58. Soderlund, U.; Patchett, P.J.; Vervoort, J.D.; Isachsen, C.E. The ^{176}Lu decay constant determined by Lu-Hf and U-Pb isotope systematic of Precambrian mafic intrusions. *Earth Planet. Sci. Lett.* **2004**, *219*, 311-324, https://doi.org/10.1016/S0012-821X(04)00012-3.
59. Blichert-Toft, J.; Chauvel, C.; Albarede, F. Separation of Hf and Lu for high-precision isotope analysis of rock samples by magnetic sector-multiple collector ICP-MS. Contrib. *Mineral. Petrol.* **1997**, *127*, 248–260, https://doi.org/10.1007/s004100050278.
60. Griffin, W.L.; Pearson, N.J.; Belousova, E.; Jackson, S.E.; Achterbergh, E.V.; O'Reilly, S.Y.; Shee, S.R. The Hf isotope composition of cratonicmantle: LAM-MC-ICPMS analysis of zircon megacrysts in kimberlites. Geochim. *Cosmochim. Acta* **2000**, *64*, 133–147, https://doi.org/10.1016/S0016-7037(99)00343-9.
61. Griffin, W.L.; Wang, X.; Jackson, S.E.; Pearson, N.J.; O'Reilly, S.Y.; Xu, X.; Zhou, X. Zircons chemistry and magma genesis in SE China: in situ analysis of Hf isotopes, Pingtan and Tonglu igneous complexes. *Lithos* **2002**, *61*, 237-269, https://doi.org/10.1016/S0024-4937(02)00082-8.
62. Sun, S.S.; McDonough, W.F. Chemical and Isotopic Systematics of Oceanic Basalts: Implications for Mantle Composition and Processes. *Geol. Soc. London Spec. Publ.* **1989**, *42*, 313-345, http://dx.doi.org/10.1144/GSL.SP.1989.042.01.19.

63. Lu, H.Z.; Fan, H.R.; Ni, P.; Ou, G.X.; Shen, K.; Zhang, W.H. *Fluid Inclusions*. Science Press, Beijing, China, 2004, pp. 1–487. (In Chinese).
64. Whalen, J.B.; Currie, K.L.; Chappell, B.W. A-type granites: geochemical characteristics, discrimination and petrogenesis. *Contrib. Mineral. Petrol.* **1987**, *95*, 407–419, https://doi.org/10.1007/BF00402202.
65. Pearce, J.A.; Harris, N.B.W.; Tindle, A.G. Trace-element discrimination diagrams for the tectonic interpretation of granitic-rocks. *J. Petrol.* **1984**, *25*, 956–983, https://doi.org/10.1093/petrology/25.4.956.
66. Oppenheimer, C.; Moretti, R.; Kyl, P.R.; Eschenbacher, A.; Lowenstern, J.B.; Hervig, R.L.; Dunbar, N.W. Mantle to surface degassing of alkalic magmas at Erebus volcano, Antarctica. *Earth Planet. Sci. Lett.* **2011**, *306*, 261–271, https://doi.org/10.1016/j.epsl.2011.04.005.
67. Lee, C.T.A.; Leeman, W.P.; Canil, D.; Canil, D.; Li, Z.X.A. Similar V/Sc systematics MORB and Arc Basalts: Implications for the Oxygen Fugacities of their Mantle Source Regions. *J. Petrol.* **2005**, *46*, 2313–2336, https://doi.org/10.1093/petrology/egi056.
68. Patino Douce, A.E. What do experiments tell us about the relative contributions of crust and mantle to the origin of granitic magmas? *Geol. Soc. London Spec. Publ.* **1999**, *168*, 55–75, http://dx.doi.org/10.1144/GSL.SP.1999.168.01.05.
69. Huang, H.Q.; Li, X.H.; Li, W.X.; Li, Z.X. Formation of high $\delta^{18}O$ fayalite-bearing A-type granite by high-temperature melting of granulitic metasedimentary rocks, southern China. Geology 2011, 39, 903–906, https://doi.org/10.1130/G32080.1.
70. Patino Douce, A.E. Generation of metaluminous A-type granites by low-Pressure melting of calc-alkaline granitoids. *Geology* **1997**, *25*, 743–746, https://doi.org/10.1130/0091-7613(1997)025<0743:GOMATG>2.3.CO;2.
71. Dall'Agnol, R.; Frost, C.D.; Ramo, O.T. IGCP Project 510 "A-type granites and related rocks through time": project vita, results, and contribution to granite research. *Lithos* **2012**, *151*, 1–16, https://doi.org/10.1016/j.lithos.2012.08.003.
72. Zhang, X.H.; Yuan, L.L.; Xue, F.H.; Zhang, Y. Contrasting Triassic ferroan granitoids from northwestern Liaoning, North China: magmatic monitor of Mesozoic decratonization and craton–orogen boundary. *Lithos* **2012**, *144–145*, 12–23, https://doi.org/10.1016/j.lithos.2012.03.022.
73. Touret, J.L.R. *Fluid inclusions and pressure-temperature estimates in deep-seated rocks*. In: Helgeson, H.C. Ed.., Chemical Transport in Metasomatic Processes. NATO ASI Series, 1987, C-218, pp. 91–121.
74. Skjerlie, K. P.; Johnston, A.D. Fluid-absent melting behavior of an F-rich tonalitic gneiss at mid-crustal pressures: implications for the generation of anorogenic granites. *J. Petrol.* **1993**, *34*, 785–815, https://doi.org/10.1093/petrology/ 34.4.785.
75. Jugo, P.J.; Luth, R.W.; Richards, J.P. Experimental determination of sulfur solubility in basaltic melts at sulfide vs. sulfate saturation: Possible implications for ore formation. *Am. Geophys. Union* **2001**, *82*, 47.
76. Kemp, A.I.S.; Wormald, R.J.; Whitehouse, M.J.; Price, R.C. Hf isotopes in zircon reveal contrasting sources and crystallization history for alkaline to peralkaline granites of Temora, southeastern Australia. *Geology* **2005**, *33*, 797–800, https://doi.org/10.1130/G21706.1.
77. Zhang, X.H.; Yuan, L.L.; Xue, F.H.; Yan, X.; Mao, Q. Early Permian A-type granites from central Inner Mongolia, North China: Magmatic tracer of post-collisional tectonics and oceanic crustal recycling. *Gondwana Res.* **2015**, *28*, 311–327, https://doi.org/10.1016/j.gr.2014.02.011.
78. Wei, R.H.; Gao, Y.F.; Xu, S.C.; Santosh, M.; Xin, H.T.; Zhang, Z.M.; Li, W.L.; Liu, Y.F. Carboniferous continental arc in the Hegenshan accretionary belt: Constrains from plutonic complex in central Inner Mongolia. *Lithos* **2018**, *308–309*, 242–261, https://doi.org/10.1016/j.lithos.2018.03.010.
79. Yuan, L.; Zhang, X.; Xue, F.; Liu, F. Juvenile crustal recycling in an accretionary orogen: insights from

contrasting Early Permian granites from central Inner Mongolia, North China. *Lithos* **2016**, *264*, 524–539, https://doi.org/10.1016/j.lithos.2016.09.017.

80. Landenberger, B.; Collins, W.J. Derivation of A-type granites from a dehydrated charnockitic lower crust: evidence from the Chaelundi Complex, Eastern Australia. *J. Petrol.* **1996**, *37*, 145–170, https://doi.org/10.1093/petrology/37.1.145.
81. Zhao, X.F.; Zhou, M.F.; Li, J.W.; Wu, F.Y. Association of Neoproterozoic A-and I-type granites in South China: implications for generation of A-type granites in a subduction-related environment. *Chem. Geol.* **2008**, *257*, 1–15, http://dx.doi.org/10.1016/j.chemgeo.2008.07.018.
82. Zhang, J.H.; Gao, S.; Ge, W.C.; Wu, F.Y.; Yang, J.H.; Wilde, S.A.; Li, M. Geochronology of the Mesozoic volcanic rocks in the Great Xing'an Range, northeastern China: implications for subduction-induced delamination. *Chem. Geol.* **2010**, *276*, 144–165, https://doi.org/10.1016/j.chemgeo.2010.05.013.
83. Chen, Y.J.; Li, N. Nature of ore-fluids of intracontinental intrusion-related hypothermal deposits and its difference from those in island arcs. *Acta Petrol. Sin.* **2009**, *25*, 2477–2508, (In Chinese with English abstract).
84. Simmons, S.F.; White, N.C.; John, D.A. Geological Characteristics of Epithermal Precious and Base Metal. *Deposits. Econ. Geol. 100th Anniv. Vol.* **2005**, 485–522.
85. Li, N.; Ulrich, T.; Chen, Y.J.; Thomsen, T.B.; Pease, V.; Pirajno, F. Fluid evolution of the Yuchiling porphyry Mo deposit, East Qinling, China. *Ore Geol. Rev.* **2012**, *48*, 442–459, https://doi.org/10.1016/j.oregeorev.2012.06.002.
86. Frost, C.D.; Frost, B.R. Reduced rapakivi-type granites: The tholeiite connection. Geology **1997**, 25, 647–650, https://doi.org/10.1130/0091-7613(1997) 025<0647:RRTGTT>2.3.CO;2.
87. Batchelor, R.A.; Bowden, P. Petrogenetic interpretation of granitoid rock series using multicationic parameters. *Chem. Geol.* **1985**, *48*, 43–55, https://doi.org/10.1016/0009-2541(85)90034-8.
88. Blight, J.H.S.; Petterson, M.G.; Crowley, Q.G.; Cunningham, D. The Oyut Ulaan volcanic group: stratigraphy, magmatic evolution and timing of Carboniferous arc development in SE Mongolia. *J. Geol. Soc. London* **2010**, *167*, 491–509, http://dx.doi.org/10.1144/0016-76492009-094.
89. Zhou, J.B.; Han, J.; Zhao, G.C.; Zhang, X.Z.; Cao, J.L.; Pei, S.H.; Wang, B. The emplacement time of the Hegenshan Ophiolite: constraints from the unconformably overlying Paleozoic strata. *Tectonophysics* **2015**, *622*, 398–415, https://doi.org/10.1016/j.tecto.2015.03.008.
90. Pei, S.H.; Zhou, J.B.; Li, L. U–Pb ages of detrital zircon of the Paleozoic sedimentary rocks: New constraints on the emplacement time of the Hegenshan ophiolite, NE China. *J. Asian Earth Sci.* **2016**, *130*, 75–87, http://dx.doi.org/10.1016/j.jseaes.2016.05.022.
91. Eizenhöfer, P.R.; Zhao, G.; Sun, M.; Zhang, J.; Han, Y.G.; Hou, W. Geochronological and Hf isotopic variability of detrital zircons in Paleozoic strata across the accretionary collision zone between the North China craton and Mongolian arcs and tectonic implications. *Geol. Soc. Am. Bull.* **2015**, *127*, 1422–1436, https://doi.org/10.1130/B31175.1.
92. Han, J., Zhou, J.B.; Wang, B.; Cao, J.L. The final collision of the CAOB: constraint from the zircon U–Pb dating of the Linxi Formation, Inner Mongolia. *Geosci. Front*. **2015**, *6*, 211–225, https://doi.org/10.1016/j.gsf.2014.06.003.
93. Litvinovsky, B.A.; Tsygankov, A.A.; Jahn, B.M.; Katzir, Y.; Be'eri-Shlevin, Y. Origin and evolution of overlapping calc-alkaline and alkalinemagmas: the Late Palaeozoic Post-collisional Igneous Province of Transbaikalia (Russia). *Lithos* **2011**, *125*, 845–874, https://doi.org/10.1016/j.lithos.2011.04.007.
94. Janasi, V.; Vlach, S.R.F.; Campos Neto, M.; Ulbrich, H.H.G.J. Associated A-type subalkaline and high-K calc-alkaline granites in the Itu granite province, southeastern Brazil: petrological and tectonic significance.

Can. Mineral. **2009**, *47*, 1505–1526, https://doi.org/10.3749/canmin.47.6.1505.

95. Wang, P.; Chen, Y.J.; Fu, B.; Yang, Y.F.; Mi, M.; Li, Z.L. Fluid inclusion and H-O-C isotope geochemistry of the Yaochong porphyry Mo deposit in Dabie shan, China: a case study of porphyry systems in continental collision orogens. *Int. J. Earth. Sci.* **2014**, *103*, 777–797, https://doi.org/10.1007/s00531-013-0982-5.